Article

Patterns

DSM: Deep sequential model for complete neuronal morphology representation and feature extraction

Highlights

- We developed deep models for characterizing complete single-neuron morphology
- Long projections of neurons are critical features for identifying cell types
- Our models can classify neuron morphologies with remarkable robustness and efficiency

Authors

Feng Xiong, Peng Xie, Zuohan Zhao, ..., Linus Manubens-Gil, Lijuan Liu, Hanchuan Peng

Correspondence

h@braintell.org

In brief

Reliable and efficient characterization of neuron morphology is crucial for determining neuron cell types, which is a key question for understanding the complex atlas of the brain. This article presents a deep learning method, deep sequential model (DSM), to characterize complete neuron morphology. The DSM model organizes neuronal topology as sequence representation and extracts defining features from neuronal projections across brain regions. The results demonstrate the performance and generalizability of DSM on multiple datasets.

Xiong et al., 2024, Patterns *5*, 100896
January 12, 2024 © 2024 The Authors.
https://doi.org/10.1016/j.patter.2023.100896

CellPress

Article

DSM: Deep sequential model for complete neuronal morphology representation and feature extraction

Feng Xiong,[1,2,4] Peng Xie,[1,2,4] Zuohan Zhao,[1,2] Yiwei Li,[1,3] Sujun Zhao,[1,2] Linus Manubens-Gil,[1] Lijuan Liu,[1] and Hanchuan Peng[1,5,*]

[1]New Cornerstone Science Laboratory, SEU-ALLEN Joint Center, Institute for Brain and Intelligence, Southeast University, Nanjing, Jiangsu 210096, China

[2]School of Biological Science and Medical Engineering, Southeast University, Nanjing, Jiangsu 210096, China

[3]School of Computer Science and Engineering, Southeast University, Nanjing, Jiangsu 210096, China

[4]These authors contributed equally

[5]Lead contact

*Correspondence: h@braintell.org

https://doi.org/10.1016/j.patter.2023.100896

THE BIGGER PICTURE Delineating the cell atlas of the brain is key to understanding intelligence. The complex and exquisite morphological patterns of neuronal cells provide structural support for signal transmission in our brains. Over the past years, a significant body of neuronal morphology data has been accumulated, raising urgent needs for computational tools to fully extract features relevant to cellular identity and connectivity. Here, we find that the long-projecting trajectory of a neuron, which has been overseen by existing algorithms, is an effective feature for cell-type definition. We utilize a series of natural language models to decipher the projection pathways and significantly improve the accuracy of neuronal type classification. Our work provides a novel quantitative strategy for creating a consensus of a neuronal cell atlas, which is potentially applicable to understanding defects in neurological diseases.

1 2 **3** 4 5 **Development/Pre-production:** Data science output has been rolled out/validated across multiple domains/problems

SUMMARY

The full morphology of single neurons is indispensable for understanding cell types, the basic building blocks in brains. Projecting trajectories are critical to extracting biologically relevant information from neuron morphologies, as they provide valuable information for both connectivity and cell identity. We developed an artificial intelligence method, deep sequential model (DSM), to extract concise, cell-type-defining features from projections across brain regions. DSM achieves more than 90% accuracy in classifying 12 major neuron projection types without compromising performance when spatial noise is present. Such remarkable robustness enabled us to efficiently manage and analyze several major full-morphology data sources, showcasing how characteristic long projections can define cell identities. We also succeeded in applying our model to both discovering previously unknown neuron subtypes and analyzing exceptional co-expressed genes involved in neuron projection circuits.

INTRODUCTION

The classification of neuronal types is crucial to understanding the complex circuits of the brain. Neuronal classification requires comprehensive characterization at the levels including morphology, electrical properties, transcriptomics, or a combination of them.[1,2] Among these, neuron morphology provides key implications for cellular identity and neuronal connectivity. However, morphological studies have long been restricted to the soma-proximal areas, being limited by the existing imaging technologies. Recently, large-scale labeling, imaging, and reconstruction technologies have enabled the characterization of complete neuron morphologies at the whole-brain level.[3,4] These studies showed cell-type diversity and sub-types observed in whole brain level provide new clues for understanding neuronal circuits.[4]

To describe complex neuron morphologies and to classify cell types, two key questions need to be addressed: feature extraction and quantitative comparison. Several feature extraction methods have been proposed, including vertex analysis,[5] fan-in analysis,[6] fractal analysis,[7] and L-Measure morphometrics.[8,9] The spatial distribution of dendritic arbors has also been demonstrated to be a relevant feature.[10] For quantitative comparison of morphological data, both supervised and unsupervised algorithms have been proposed.[11,12] However, these approaches are designed for analyzing dendrites and local axons arbors and the extracted features may not be suitable for characterization of morphologies with long-range projections.

In recent years, several methods have been proposed for studying the full morphology of projecting neurons. Considering the spatial distribution of both local and distal neuronal branches, NBLAST was designed by Costa et al.[13] for measuring pairwise neuronal similarity. Integrating topological branching patterns with spatial information, persistent homology was introduced to compare neuron structures and classify a large collection of neuronal structures.[14,15] BlastNeuron compares morphological similarities using a structural alignment approach.[16] However, the accuracy and robustness of such approaches are considerably affected by within-type diversity and registration precision.

The long-range projection path is a biologically relevant feature for defining cell types,[4] which is neglected by the abovementioned approaches. Here, we propose a strategy to encode the projection path, a tree-like structure of 3D coordinates in the brain space, as a computable characteristic for quantitative analysis. We organized the neuronal tree topology as a sequence representation, which was used for identification of structural motifs.[17,18] The sequence structure provides a natural representation of the projection orders and allows for the application of a series of deep sequential models (DSMs). For cell-type classification tasks, we implemented and trained a hierarchical attention network[19] model (DSM-HAN) and demonstrated its outstanding performance. For the measurement of cell-cell similarity, we trained a sequential autoencoder model (DSM-AE) to give each cell a concise representation, which encoded information of both projection strength and order of innervated brain regions. We showed the usage of DSM-AE in unsupervised clustering and automated cell-type annotation of large datasets. With DSM-AE feature encodings, we built a database and provided an online service for fast retrieval of neuron morphologies and cell-type annotation.

RESULTS

Overview of the model structure, datasets, and applications

To extract features and characterize neuronal morphologies, we constructed several DSMs, serving for multiple applications (Figure 1). We built a pipeline for preprocessing and feature extraction for neuron reconstruction (Figure 1A). The original input is the digital reconstruction of neuronal morphology, including the complete long-range projection. Reconstructed neurons were registered to CCF reference space[20] after which each segment of the reconstruction belongs to a certain brain region according to its 3D location in the space. We applied a depth-first traversal algorithm to convert the tree structure of the morphologically reconstructed neurons into a sequence of brain regions (see experimental procedures), where each node in the sequence is represented as a one-hot encoding. The designed traversal order makes child branches close to their parent branches, allowing for more compact sequentialization of the local morphologies along the projection path. Each node is assigned to one of 316 manually curated non-overlapping brain areas[21] with highly variable spatial proximity and functional properties.

To reduce redundancy of the one-hot encoding vectors, we introduced the word2vec (W2V) module[22] (see experimental procedures) for feature compression and extraction. We applied this model to over 1,000 neurons of multiple types and found that W2V is not only able to convert the 316-dimension vectors into dense vectors, but also enhances the robustness of feature representation. Thus, we used the W2V module to generate the input for both supervised classification and unsupervised representation (Figure 1B).

The DSM consists of two downstream models, DSM-HAN and DSM-AE, performing supervised classification and unsupervised representation separately. In the supervised module, a hierarchical attention network is adopted as DSM-HAN for cell-type classification. DSM-HAN reviews neuron morphologies in a hierarchical manner including node level, segment level, and the neuron level, providing both segment-level encodings and neuron level encodings. The model shows its interpretability by encoding neighboring segments into similar vectors (Figure S1). We trained the DSM-HAN model with 1,282 neurons that belong to 12 cell types (caudate putamen substantia nigra pars reticulate [CP_SNr], caudate putamen globus pallidus externa [CP_GPe], ventral posteromedial nucleus of the thalamus [VPM], extratelencephalic somatosensory cortex [ET_SS], intratelencephalic somatosensory cortex [IT_SS], ventral posterolatral nucleus of the thalamus [VPL], dorsal part of the lateral geniculate complex [LGd], medial geniculate complex [MG], intratelencephalic visual area [IT_VIS], intratelencephalic motor cortex [IT_MO], thalamic reticular nucleus [RT], and extratelencephalic motor cortex [ET_MO]) from a dataset recently obtained by our team.[4]

In the unsupervised module, we trained a DSM-AE model for data exploration, including unsupervised clustering and retrieval of similar morphologies. Details of the W2V model and DSM are introduced in the following sections.

W2V: Distributed vectors of brain regions

In this study, we propose a strategy to utilize brain regions, to help identify the cell types. Sub-regions within one major brain region, such as the somatosensory cortex, may share functional, spatial, and developmental similarity. Thus, neurons projecting to these closely located sub-regions might belong to the same cell type (e.g., VPM neurons may project SSp-m or SSp-bfd).

To determine the projection regions, the registration of neuron reconstructions from different brains can also introduce certain levels of error. In addition, current characterization for brain regions is not only lack of connectivity profiles, but also cannot reach the single-cell resolution. We can address these concerns by proposing the feature, our brain region encodings. The feature is produced by the W2V algorithm, which is a classic method for feature extraction and compression in NLP tasks.[22] Since our neuron morphology is converted into sequences, it provided the facility to embed nodes (brain regions) from the sequences. W2V assigns each node with a unique encoding (fixed-length

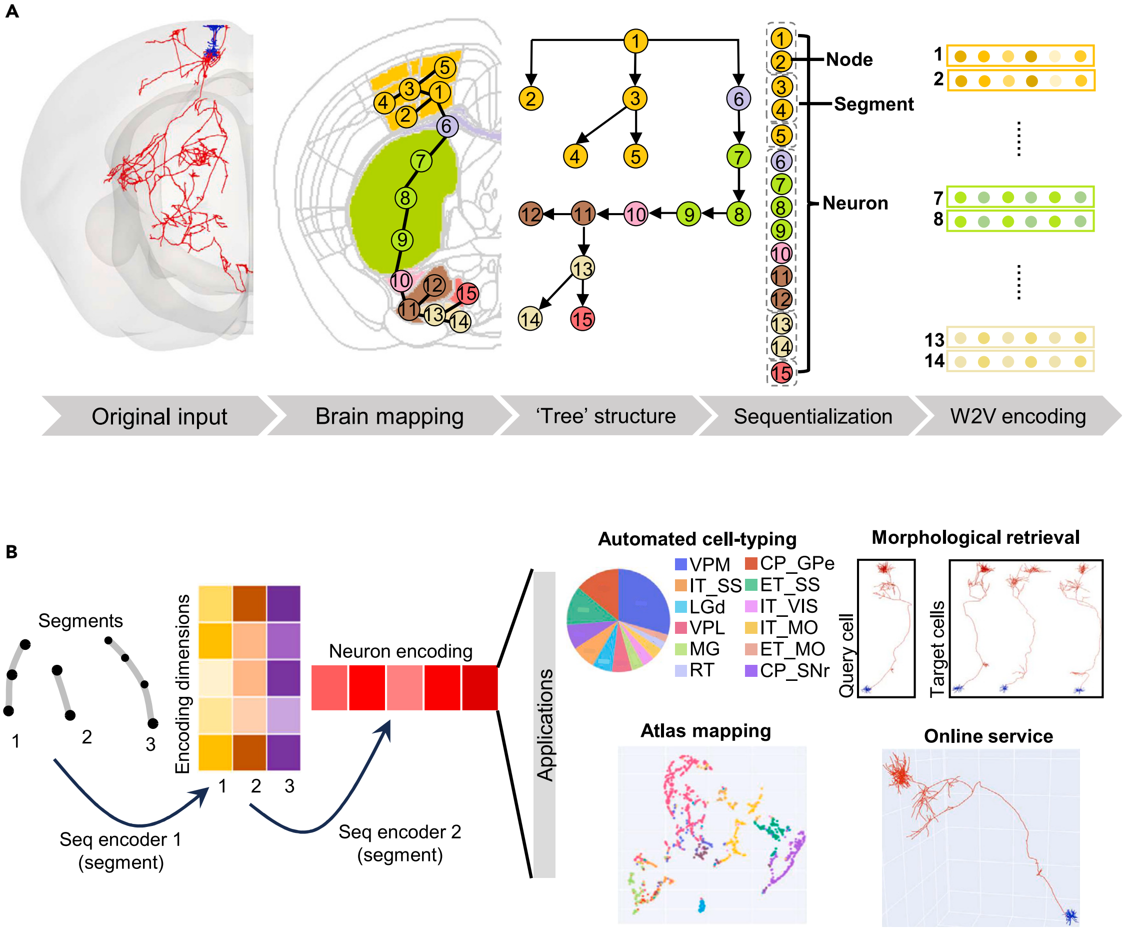

Figure 1. Overview of the sequential model and its applications

(A) Raw data transformation process including mapping the nodes of reconstructed neurons to brain regions, tree structure representation, depth-first search, which disassembles the tree structure as segment sequences, and word2vec (W2V) encoding that represents each node as the embedding of its brain region.

(B) Neuron encoding process. A neuron is encoded by two steps of recursive neural network transformation. This process encodes neurons with variable sizes as a vector of the same dimensions, which is then used as input for automated cell-type classification, unsupervised atlas mapping, and morphological retrieval.

vectors) indicating its semantics such that nodes with similar semantics or synonymous have closer encodings. By applying W2V, we were able to encode brain regions as dense vectors, reflecting their functional and spatial similarity, which benefits the downstream analysis.

Our W2V neural network is composed of three layers, including an input layer, a hidden layer, and an output layer, as shown in Figure 2A. The input and output data are one-hot encodings of brain regions. Fed with the sub-sequence of context nodes as input, the model predicts the one-hot encoding of its center node. The dense encoding of center node comes from the average hidden layer representation of input nodes (see Table S1 for model parameters; see experimental procedures). The training process minimizes the prediction error of the center node.

To enhance the robustness of the W2V, we generated an augmented dataset by introducing Gaussian noise to node coordinates and used it as the training data of W2V (see experimental procedures). The augmented dataset contains 316 brain regions and 5,370 cells. These brain region embeddings can be grouped as 6 major brain regions: cerebral nuclei, cerebral cortex, thalamus, midbrain, hypothalamus, and hindbrain. After training, each brain region was encoded as a 6-dimension embedding vector (Table S2). The dimension of W2V encoding was chosen by the least training loss of W2V (Figure S2A). Dimension reduction (t-SNE) of these W2V encodings shows that the 316 sub-regions within the same major brain regions are clustered together (Figure 2B).

HAN: Supervised cell-type classification

For supervised morphological classification, we adopted a DSM-HAN model, which was originally used for document classification.[19] The intuition is to treat a neuron sequence (a sequence of W2V-encoded brain regions) as a document (a sequence of words), and treat neuron segments (sub-sequences) as sentences. The DSM-HAN architecture reviews the sequence and extracts features following the order of nodes to segments and segments to neurons. W2V encodings of nodes in the same segment are seen as independent sub-sequences, representing local morphologies. The node-level network takes

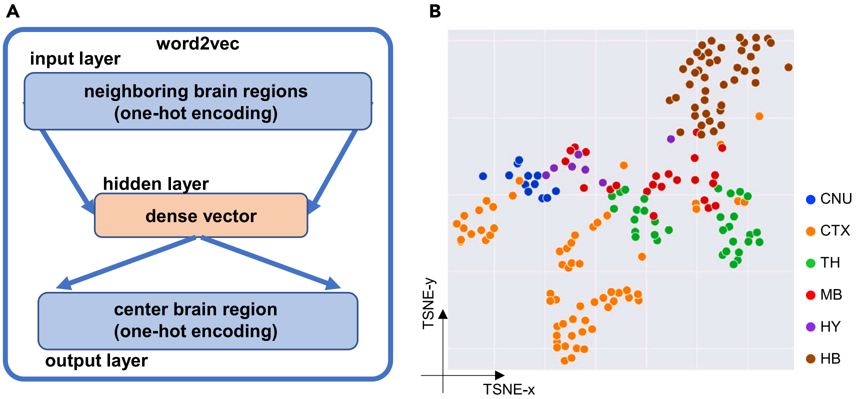

Figure 2. Word2vec: Distributed vectors of brain regions

(A) Word2vec network structure.

(B) Distribution of trained brain regions in a t-SNE layout. To display the training result, sub-regions are separated into six major regions: CNU (cerebral nuclei), CTX (cerebral cortex), TH (thalamus), MB (midbrain), HY (hypothalamus), and HB (hindbrain). Structures belonging to the same major region are displayed in the same color. Each dot represents a sub-region reduced from W2V encodings, and the colors indicate the major brain regions.

these W2V encodings as input, integrating the information within the sub-sequence. Its output, the node-wise averaged attention encodings, referred to as segment encodings, are passed to the segment-level network. We implemented a similar structure for the segment-level network, which integrates segment-level encodings. At the whole-neuron level, we implemented a fully connected layer to output the probability estimation of cell types (Figure 3A; see experimental procedures). Key hyperparameters of the model include the sizes of hidden layer dimensions of W2V and HAN, segment number, and segment length. Settings of hyperparameters are detailed in Figure S2 and Table S1.

We trained and tested the DSM-HAN model on a dataset with 1,282 neuron cells from 12 manually assigned types based on their soma locations and projecting brain structures (Table S3). We used 80% of the data (1,025 cells) for training and the remaining 20% (257 cells) for testing. Through 30 independent training sessions (random sampling of training and testing data), the model achieved 92.76% average testing accuracy. The high class-wise area under the curve (>0.98 in all cases) scores of the receiver operating characteristic suggest high robustness (Figure 3B). We performed ablation studies to test the necessity of using the complex DSM-HAN model. Simpler models including multilayer perceptron and random forest were operated on the flattened W2V encodings (Figure S3), receiving average test accuracy of 36.52% (random forest) and 83.50% (simple multilayer perceptron). The results indicate DSM-HAN as a superior module for classifying neuron sequences.

The information of the input neuron sequences was encoded from two features: the residing brain regions of nodes and their sequential orders. We performed tests to examine whether DSM-HAN was able to learn sequential information that was independent from brain regions. At the segment level, we performed hierarchical clustering for the segment encodings and identified the top 2 clusters for each cell (Figure S1). Segments with close sequential orders were clustered together regardless of the residing brain regions, even for neurons with multiple target regions (e.g., ET_MO neurons). At the neuron level, we reversed sequence orders for each cell and performed clustering together with the original sequences (Figure S4). For most cell types, the reversed and original sequences form distinct clusters, and one sample discriminability tests[23] (see experimental procedures) indicate clear separation in their native embedding space (Figure S4). The only exceptions were found for IT neurons where the segments' residing regions are highly invariable. These results indicate that DSM-HAN utilizes the sequential information of projection orders, which further influence the neuron encodings.

We compared the model performance with alternative methods including TFIDF, graph convolutional network (GCN), TextRNN, TextCNN, NBLAST, Sholl analysis, L-Measure, and topological morphology descriptor (Figure 3C). TFIDF is a classic sequential model widely used for feature extraction in document classification.[24] TFIDF was applied to extract features from neuron sequences, making the dataset a "number of cells" by "number of unique brain regions" matrix (see experimental procedures). We obtained an average testing accuracy of 89.29%. Alternatively, GCN[25] presents a simple network utilizing a graph structure of data, achieving great classification results on tasks, such as node classification, relation classification, etc. We used the tree structure of neurons as the graph, and the brain region (W2V encodings) as input features, achieving a testing accuracy of 91.02%. TextRNN and TextCNN are both deep models for text classification, and one uses recurrent neural network [RNN] as basic feature extractor, the other uses CNN.[26,27] Using the W2V encodings, the testing accuracy is 85.67% for TextRNN and 86.12% for TextCNN. NBLAST calculates the spatial proximity between neuronal segments through structural alignment.[13] We used NBLAST similarity matrix values as input features for several machine learning algorithms, among which linear-kernel SVM showed the best testing accuracy (72.74%). Sholl analysis characterizes the spatial branching pattern of a neuron by counting the number of its intersections with concentric spheres centered by the soma. We used the intersection profiles as features (see experimental procedures), and trained linear-kernel SVM classification models, showing an average testing accuracy of 66.08%. We used morphological features (see experimental procedures) summarized by L-Measure to characterize neuron morphologies and trained linear-kernel SVM for classification (average testing accuracy, 71.88%). The "persistent homology" analysis couples morphology properties and neuron branching patterns,[14] which is also known as topological morphology descriptor[15] (TMD). The radial distance of current node to soma is chosen as the description function to convert neuron structures to persistent diagrams, characterizing neuron morphologies. We obtained average testing accuracy with linear-kernel SVM (68.43%). For each alternative method, we divided training and testing datasets using the same strategy as for DSM-HAN and trained classification models through 30 independent training sessions. Comparison of testing accuracy

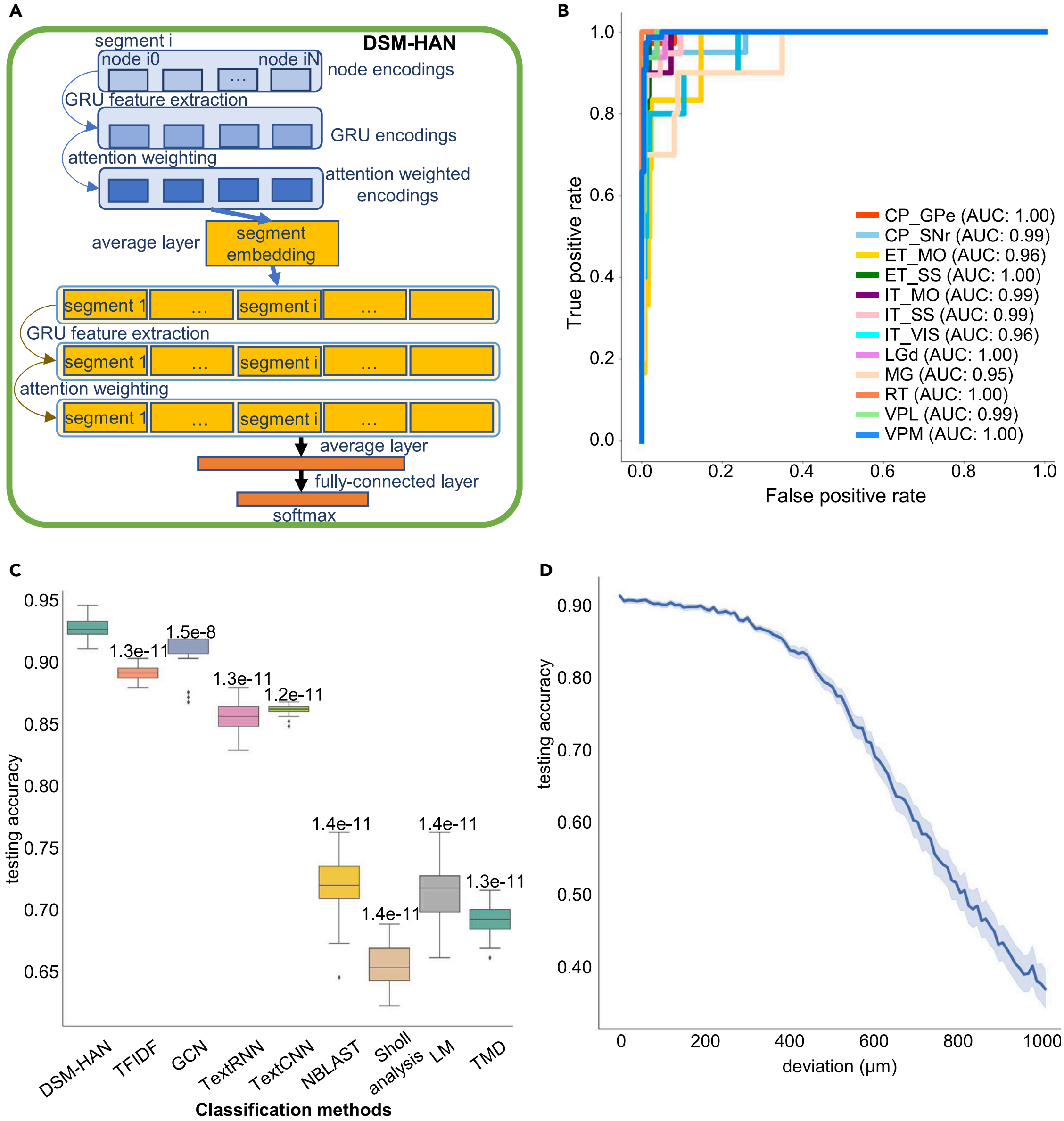

Figure 3. Hierarchical attention network: Supervised cell-type classification

(A) Hierarchical attention network structure. Blue blocks: node-level neural networks. Yellow blocks: sentence-level neural networks. Orange blocks: neuron-level neural networks.

(B) The receiver operating characteristic (ROC) curve and area under the curve of the DSM-HAN classifier. Taking multi-class classification as 12 binary classifications, we calculated false positive rate and true positive rate for each binary classification and plot the ROC curves. The ROC curve of each type is displayed in one color.

(C) Comparison between methods. Each method was tested by 30 times of cross-validation, and results are displayed by boxplots (numbers above box: p values of the Mann-Whitney U rank test (one-side) on test accuracy between DSM-HAN and others).

(D) Robustness test: the testing accuracy for noise levels ranging from 10 to 1,000 μm. The accuracy curve is aggregated over repeated values (each noise level with 30 independent trainings and testings), showing the mean testing accuracy and 95% confidence interval.

indicates the significant outperformance of DSM-HAN over alternative methods (Figure 3C).

To investigate the effectiveness of our brain region encodings (from the W2V model), we compared it with direct node coordinates (x-y-z) in the supervised cell-type classification. The two sets of features are tested using both the DSM-HAN and GCN models, and results show the advance of our brain region encodings over node coordinates in both models (Figure S5).

To investigate the generalizability of DSM-HAN for morphological data, we tested its performance for alternative datasets, including a newly released full morphology dataset[28] with 11 cell types (mostly different from the 12 cell types of the SEU dataset[4]) and local morphologies (dendrites) from the SEU dataset

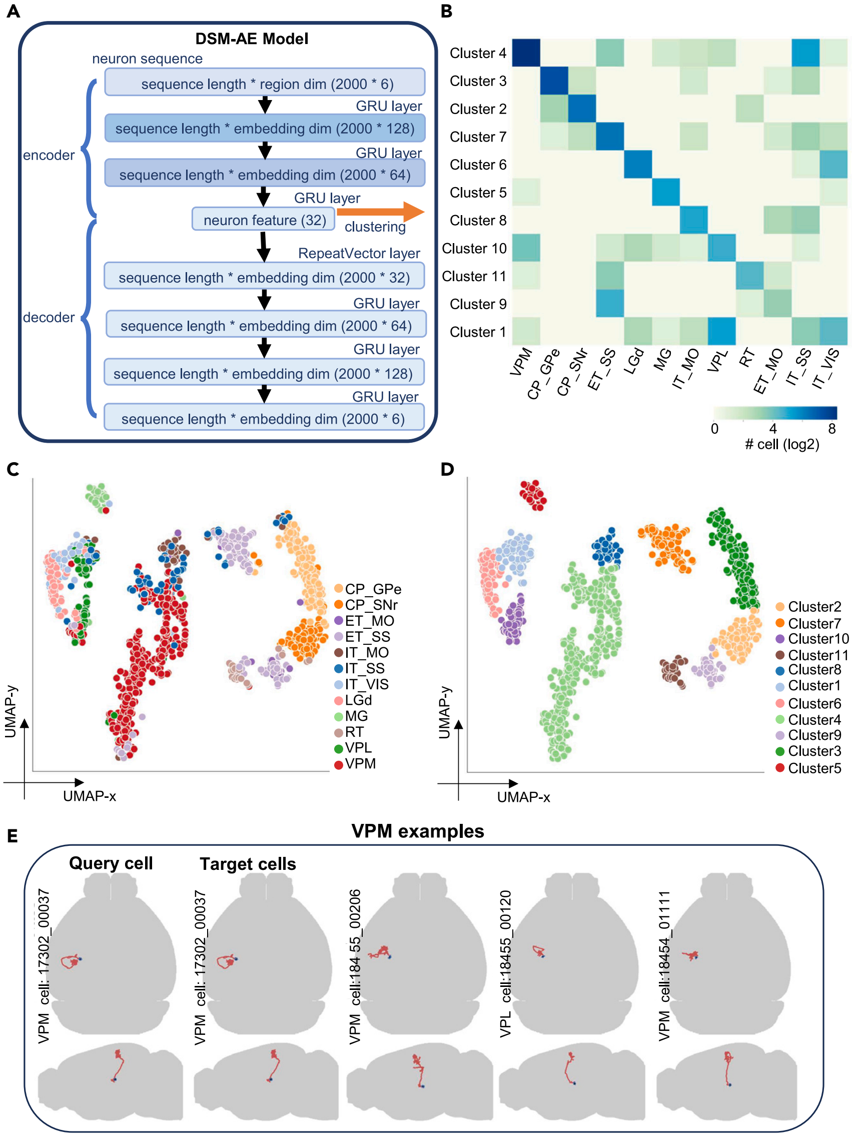

Figure 4. Autoencoder: Concise representation for exploratory studies and data retrieval

(A) DSM-AE network structure.

(B) Confusion matrix of clusters and cell types. The color bar indicates the 2-based logarithm of cell numbers.

(C) Data visualization of the DSM-AE encoding. The neuron sequences are encoded as 32-dimension vectors and projected to 2D space by the UMAP algorithm. Colors indicate cell types (left) or the DBSCAN cluster assignment (right). Only cells above DBSCAN confidence threshold are shown.

(D) Morphological data retrieval. The brain-level views of query cells and target cells are reported by the online service.

(see experimental procedures). DSM-HAN achieved 92.2% testing accuracy for the 11-cell-type dataset and UMAP of the hidden layer encodings shows distinct separation between cell types (Figure S6). For classification of dendrites, DSM-HAN outperformed alternative methods (Figure S7), although its performance (testing accuracy = 76.4%) was lower than that in the classification tasks of long-projecting neurons. The reduced accuracy can be explained by the highly similar sequence encodings of dendritic types from the same brain regions (e.g., IT_MO and ET_MO). The performance can be further improved by refined brain region assignment (e.g., dividing cortical regions by layers; Figure S7), reaching to 84.7%.

To test the robustness of the DSM-HAN model to the registration deviation, we introduced Gaussian noise to the node coordinates of the testing dataset (257 cells). This perturbation resulted in changes to the brain region assignment of many nodes. The noise level (the standard deviation of Gaussian distribution) was gradually increased from 10 to 1,000 μm, with a 10 μm step size (Figure 3D). Results show that the testing accuracy was stably high (>90%) with a noise level <200 μm. Empirically, the maximum registration deviation for mouse brains is 100 μm.[29] Thus, the DSM-HAN model is robust to variations introduced by registration and brain region assignment. We further test the robustness of all alternative approaches. Results show that TFIDF and NBLAST were able to maintain their accuracy under spatial noise <100 μm, while the performance of others fell dramatically with increased noise (Figure S8).

Autoencoder: Concise representation for exploratory studies and data retrieval

Direct cell-cell comparison is important for exploratory studies and data retrieval. As there is no exact node-to-node correspondence between two different neuron reconstructions, it becomes necessary to generate comparable and quantitative representations for them. Here, we adopted a sequence autoencoder as the DSM-AE model. This model aims to learn a latent vector representing input neuron sequence and recover the input sequence from the latent vector (see experimental procedures). The training process optimizes parameters of the model to minimize the difference of recovery and input sequence. Thus, the latent vector representation significantly reduces the data dimensionality while retaining most of the projection information.

For applicability evaluation, we applied the model to the 1,282-cell dataset of 12 cell types (see experimental procedures) and generated their DSM-AE representations. DBSCAN[30] (see Figure S9 for parameter determination policy) was operated on tSNE-transformed DSM-AE representations to identify 12 clusters. We used the adjusted Rand index (ARI) to measure the correspondence between clusters and cell types (ARI = 0.719; Figure 4B). We used the discriminability metric[23] to measure the separation of 12 cell types in the t-SNE-transformed embedding space (discriminability = 0.888). 2D visualization of the DSM-AE encoding shows that cells from the 12 different classes form distinct sub-populations and the distribution of the clusters match the manually defined projection-based groups (Figures 4C and 4D).

For comparison, we applied the same procedure to evaluate alternative approaches including TFIDF, NBLAST, Sholl analysis, L-Measure, and TMD. We also performed the evaluation for the direct W2V sequence representations (see experimental procedures). To eliminate the possible effect of post-processing methods operated on the native representations, we calculated ARI and discriminability under a variety of post-processing procedures, including standardization, PCA, tSNE, UMAP, ISOMAP, MDS, and LLE (see experimental procedures). For both ARI and discriminability, DSM-AE demonstrated outperformance and higher robustness over alternative approaches, under all post-processing procedures (Table S4).

For exploratory studies in which the number of cell types are unknown and novel cell types may exist, DSM-AE can be combined with DSM-HAN for automated dataset annotation. For identification of novel cell types, we introduced an outlier detection module with 12 outlier detectors. For each known cell type, a detector is a one-class SVM model using DSM-AE encodings as input data (see experimental procedures). After a cell is assigned to a cell type by DSM-HAN, the corresponding detector is applied, and changes its label to "unknown" if the cell is found to be an outlier. As a proof of concept, we applied this approach to the annotation of an external set of full morphology neurons (Janelia dataset; 1,002 neuron cells[3]), 61% cells of which belong to novel cell types (Table S5). We evaluated the outlier detection performance by comparing its predictions with the manually curated labeling. The median of F1 score was 0.54 (VPM = 0.71; VPL = 0.33; IT_MO = 0.85; ET_MO = 0.72; IT_VIS = 0.55; ET_SS = 0.07; IT_SS = 0.38). We examined poorly performing detectors and found that most of the cells were assigned to cell types with similar morphology (e.g., VPM assigned as VPL, ET_MO assigned as ET_SS). We summarized the training and testing results in Table S6.

The DSM-AE representations are further reduced to 2D using a UMAP algorithm, resulting in a 2D reference atlas. User-uploaded morphological data (query data) are projected to the 2D reference atlas for determining cell types according to the similarity with reference data points. In addition, the most similar single cells (target data) and their horizontal/vertical views are reported for visual inspection (Figure 4D). Also, more examples including the least similar cells from non-target neuron classes are also provided, demonstrating the diverse morphological types in the dataset (Figure S10). The website (see data and code availability) also provides a series of tools including interactive visualizations of W2V brain region encodings, 2D reference data atlas, and 3D single-cell morphologies.

Subtyping of neurons cross-validated by analysis of projection patterns

It is intriguing to explore previously unknown sub-types of cells. To examine whether the DSM-AE model may facilitate the discovery of neuronal sub-types, we cross-validated it with third-party neuron morphology datasets. Particularly, we focused on two major brain structures: the orbital area, lateral part ORBl, and the infralimbic area (ILA). For each of them, we trained a DSM-AE model that characterized cells with 32-dimension embeddings. These embeddings formed distinct sub-populations (Figure 5A), suggesting different previously unknown sub-types in the respective cell class. We cross-validated these sub-types of cells by examining their projection strength patterns manifested by the respective axon length calculated from neuron reconstructions in a recent independent study[28] in target brain regions. We found clear clustering patterns (Figure 5B). Our results show high reliability of the DSM-AE sub-types (ORBl: ARI = 0.989; ILA: ARI = 0.381; Table S7). Visual inspection of the 3D morphology of example neurons also confirmed these sub-types (Figure 5C).

We applied the same procedure to explore morphological variations in all the 12 cell types from the SEU dataset. The region-wise projection strength drove the clustering results for most cell types (e.g., IT_SS cells clustered by projections in sub-regions such as SSp-bfd and SSp-m; Figure S11). Unlike the ORBl and ILA types where distinct sub-clusters were identified, most of the 12 cell types were less heterogeneous and showed continuous distributions in the embedding space. In addition to variations in projection strength, DSM-AE was able to capture essential characteristics of cell identity. For example, re-clustering of IT_SSp-bfd neurons demonstrates a morphological continuum where L2/3, L4, and L5 cells are distributed in different portion. A similar pattern was observed for the IT_SSp-m neurons (Figure S11).

Analysis of co-expression genes in connected brain regions

Spatial gene expression analysis has provided insights to resolve the organization of functional neural circuits.[31,32] The complexity of 3D gene expression distribution was previously studied from the perspective of cell types and brain regions.[31] As the gene expression of any brain area is affected by local cell bodies as well as the neurites from distal projecting neurons, it is of great importance to examine the contribution of brain-region connectivity to the spatial gene expression pattern. To our knowledge, such analysis has not been reported, likely being limited by the lack of clear definition of brain connectivity. Here, we propose to identify inter-connected brain regions using cell types defined by our DMS method. We first applied DMS-AE and DBSCAN to the 1,282-neuron dataset, identifying 11 clusters (see experimental procedures). For each cell type, we defined the projecting source and target regions as "inter-connected" (Figure 6A; see experimental procedures). Then we integrated the cell-type-level connections to generate a joint connectivity matrix, which can be combined with spatial gene expression data for further analysis (Figure 6B; see Table S8 for the connectivity matrix).

With the connectivity matrix, we asked whether inter-connected brain regions tend to show similar expression patterns. We identified expressed genes across these brain regions using the Allen Brain Atlas[21] and obtained a region-wise gene expression matrix that showed co-expression modules among neighboring regions from the same major brain regions (Figure 6C; see experimental procedures). We defined the co-expression score as the Jaccard similarity coefficient between the expressed gene sets of any two regions (see Table S9 for the co-expression matrix). Connected region pairs had substantial co-expression

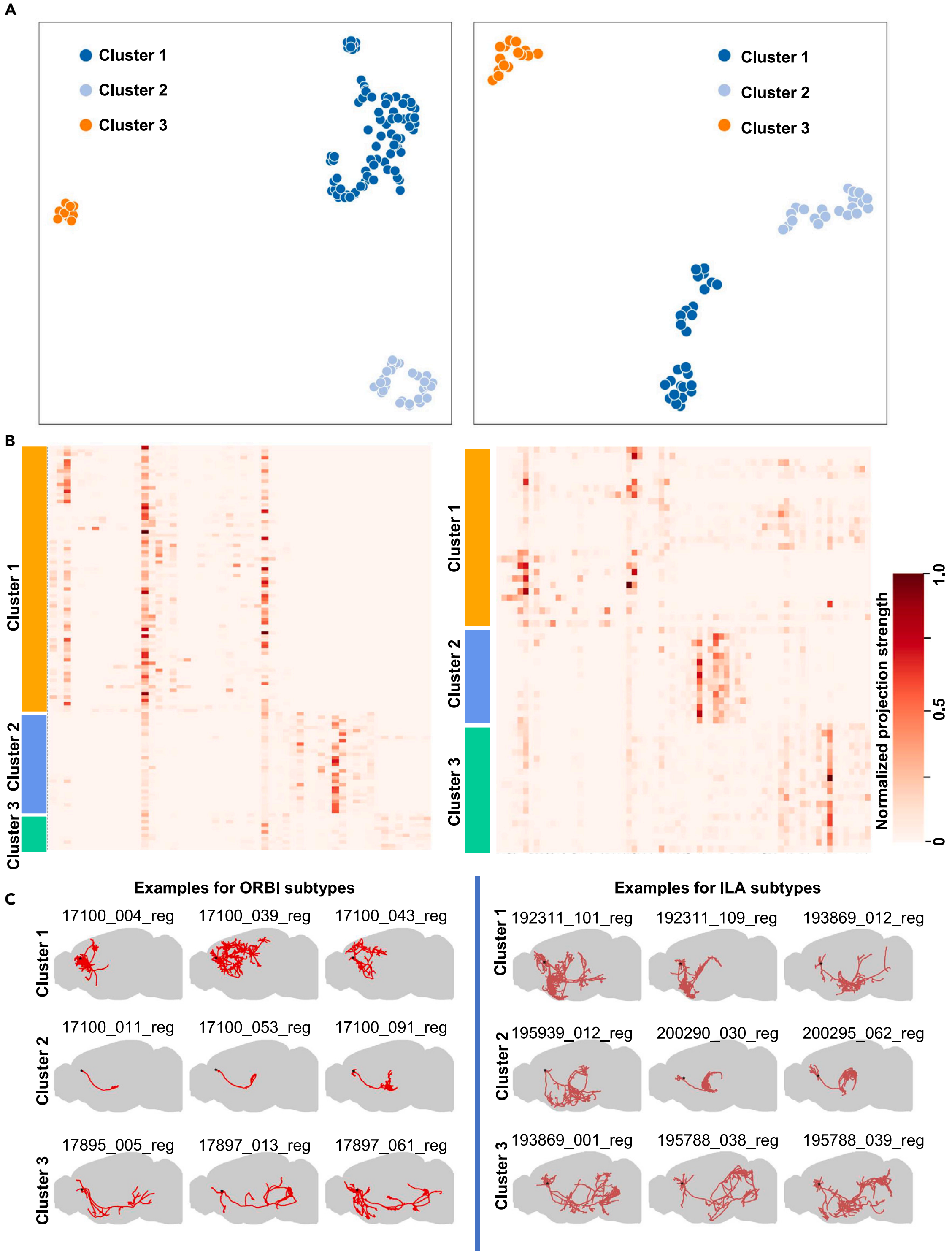

Figure 5. Sub-typing of neurons cross-validated by analysis of projection patterns

(A) Cell sub-typing derived from DSM-AE embedding (left, ORBI cells; right, ILA cells).

(B) Projection patterns of DSM-AE sub-types. Rows, cells grouped by DSM-AE clustering; columns, target brain regions. The projection strength was defined as the axon length in target brain regions normalized between 0 and 1.

(C) Visualization of neuronal axon reconstructions of three examples for each DSM-AE sub-type.

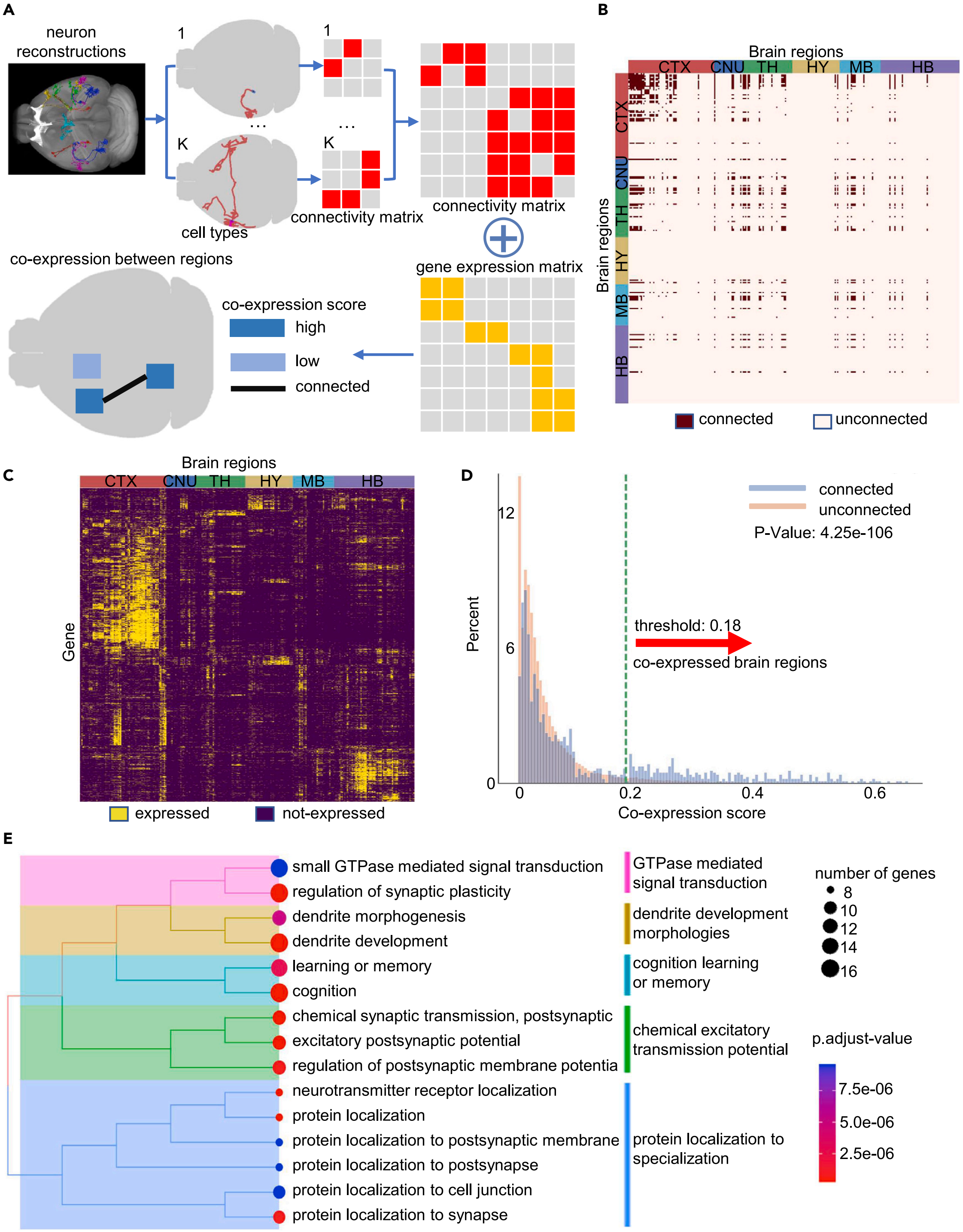

Figure 6. Analysis of co-expression genes in connected brain regions

(A) Illustration of a pipeline of co-expression analysis with the following steps: (1) input data as the morphology of 1,282 neurons, (2) identification of cell types using our DMS method, (3) determination of connected brain regions at cell-type levels, (4) combination of connectivity matrix and gene expression matrix at the whole-brain level, and (5) comparison of co-expression scores between connected and unconnected regions.

(B) The brain-region-wise connectivity matrix. Rows and columns indicate brain regions grouped by their major brain regions, including CNU (cerebral nuclei), CTX (cerebral cortex), TH (thalamus), MB (midbrain), HY (hypothalamus), and HB (hindbrain).

(C) The binary gene-by-brain region expression matrix. Colors indicate identified gene expression state (see experimental procedures).

(legend continued on next page)

scores (p = 4.25e−10^{6}, two-sided KS test; Figure 6D). Similar co-expression patterns were observed even when we excluded region pairs from the same major brain region (p = 2.92e−24, two-sided KS test; Figure S12A) to avoid the effect of co-expression between neighboring regions. We selected 2,251 connected region pairs whose co-expression scores were above the 95th percentile of unconnected ones (Figure S12B and Table S10). We found that the co-expression genes of the 2,251 pairs were highly enriched in top-row functional terms including synaptic specification, dendrite development, and cognition (Figure 6E). Synaptic transmission has been reported as an over-represented gene set that supports both structural and functional inter-regional connectivity.[33,34] Our analysis identified brain-specific angiogenesis inhibitor 1-associated protein 2 (Baiap2) as the most frequently co-expressing gene between connected regions. BAIAP2L2 (a paralog of BAIAP2), which induces planar or curvature membranes, was previously reported to be reflective of structural connectivity of human brains.[35] Among the top 200 regional co-expressing genes, we also identified genes related to ion channels (Camk2a, Camkk1, Kcnj4), neuronal process formation (Enc1), and neurotransmitters (Syt16). Remarkably, a general survey of expressed genes in the brain atlas suggested more broad functional terms including organelle localization, histone modification, and signal transduction (Figure S12C). Compared with these broader "background" functions that might be contributed by "housekeeping" genes or non-neuronal cell types in the brain,[31] our results in Figure 6E suggest previously unreported patterns that cell-type-specific brain connectivity is influential to the spatial gene expression, likely through the co-expression of genes that support neuron-specific functions.

DISCUSSION

Complete morphology of long-range projecting neurons is crucial for deciphering the diversity of cell types and for understanding organizational principles of brain connectivity. The unique and complex nature of morphological structure implies difficulties for data analysis. In this work, we introduce a sequential model for feature extraction from full neuronal morphology, which enables efficient cell-type classification, morphological clustering, and data retrieval. We provide a series of computational tools that outperform existing ones in accuracy and robustness. These tools are available as online services for researchers with or without computational backgrounds.

Compared with the transcriptome data based on gene sequencing, it is challenging to define morphological features that effectively represent cell-type-related characteristics. Although some feature sets (e.g., L-Measure[9]) are more influential, there is limited consensus on a reasonable practice for feature definition. In previous studies, we defined cell types by where their projection initiates and terminates.[4] Such projections form directional trajectories in the brain, which turned out to be highly consistent within a cell type. The data structure of such trajectories shares a lot of similarities with texts, the basic structure of which is also arrays of nodes. For a paragraph of text, a node is a word. For the morphology of a neuron, a node is a point along a branch. Such arrays are logically (for texts) or physically (for neurons) connected, forming branching structures. In the field of natural language processing, a series of classical techniques enable tasks including texts understanding and generation. The similarity of data structure renders NLP techniques applicable for the study of neuronal projection paths.

Characterization of single-neuron morphologies provides valuable insights for the understanding of neural circuits. Like single-cell transcriptomes, analysis of neuronal morphologies at the level of clusters formed by similar cells is crucial for information mining. In this study, we demonstrate the application of our DSM model in finding new sub-types and the results were consistent with double-blind classification by experts. The identified sub-types may serve as anchors for crossmodality comparisons to achieve comprehensive definition of cell types. Accurate morphological classification also provides an appropriate granularity for crossmodality joint analysis. In this study, we used DSM-identified morphological clusters to define brain region connections, which avoided the lack of resolution at population level and susceptibility to false positives at the single-cell level. The inter-connected regions show significantly higher levels of gene co-expression, which is valuable to explain spatial gene expression data from the perspective of neural connections. More biological insights might be revealed by combination with spatial gene expression data at the single-cell level.

Although our sequential representation and deep learning models showed high performance in the morphological classification tasks, several limitations and future improvements are worth noting. First, the method is specifically designed for long-range projecting neurons. It is not applicable for the classification of neurons without long-range projections (e.g., most interneurons). Second, our model neglects some local morphological features (e.g., segment curvature, branching angle, etc.), which also potentially bear information of cell identity.

There are several future directions related to our model. First, motif analysis is a classical approach in the study of DNA sequences. It is interesting to identify repetitive and characteristic sub-structures of a cell type that might be related to both neuronal identity and development history. Second, the DSM enables the possibility of cross-species comparison. A metaphor for this is comparing articles written in multiple languages. The W2V model enables identification of paralogs of brain regions and the projection path analysis enables comparison of cell-type paralogs. This will be made possible with the availability of full-morphology data from other species, the most possible one being the monkey in the future.

EXPERIMENTAL PROCEDURES

Resource availability

Lead contact

The lead contact for this work is Hanchuan Peng (h@braintell.org).

(D) Histogram for co-expression scores of connected and unconnected brain regions (Kolmogorov-Smirnov two-sided test). Red arrow: the 95th percentile of unconnected regions.

(E) Functional enrichment analysis of co-expression genes between the 2,251 connected region pairs with high co-expression scores. GO tree plot results show the clustering of the top 15 enriched functional terms (adjusted p values, hypergeometric test, "BH" correction).

Materials availability

This study did not generate new unique materials.

Data and code availability

The codes, preprocessed data files, and supplemental files are archived on the Zenodo repository (https://doi.org/10.5281/zenodo.8186904 https://zenodo.org/record/8188431).[36] We also provide a python package integrating DSM models, which can be easily installed by a "pip install DSM-tools" command; source codes are also provided on Zenodo. To visualize neuron morphology and retrieve neurons based on morphological similarity, we provide an open-source online service.[36]

Transform neuron topological structure to sequence

Tree-like structures can be transformed into sequences through tree traversal algorithms. Here, to make the local morphologies a continuous sub-sequence and unfold these local morphologies along the neuron projection (from soma to distal arbor), we apply a depth-first traversal algorithm with designed traversal order.

While the soma node is the only node that could have more than two child nodes, to avoid multifurcations the soma node is discarded from the neuronal structure in advance, and its removal converts the neuron structure into several binary trees. Afterward, we apply depth-first traversal strategy on each tree to generate the corresponding sequences and concatenate them into one sequence representing the full neuron structure. This depth-first search strategy keeps adjacent connected nodes in the tree structure as close as possible in the sequence representation. The rules for traversal were set as follows: subtrees with fewer leaf nodes and shorter path are visited first. Upon iterative traversal through the tree nodes, we append each visited node to the sequence. Finally, instead of using a series of spatial coordinates directly, we encode each node with the ID of the brain region where it is located in the Common Coordinate Framework v.3 (CCFv3) 3D reference space[20] (resolution, 25 μm).

Preparation and pre-processing of dataset

The major classification and clustering tasks are conducted on a dataset of 1,282 neuron cells with labels, including 12 classes determined by their projection path in the CCF brain. Original reconstructed neurons have been published in our previous work (SEU dataset),[4] and preprocessed datasets were stored in the Zenodo repository.[36] The classes consist of CP_SNr (100 cells), CP_GPe (180 cells), VPM (378 cells), ET_SS (159 cells), IT_SS (97 cells), VPL (80 cells), LGd (78 cells), MG (50 cells), IT_VIS (48 cells), IT_MO (48 cells), RT (33 cells), and ET_MO (31 cells).

The local morphologies (dendrites) dataset also come from the separation of local dendrites from the full morphologies in the same 1,282 neuron cells including the same 12 classes.

For the newly released dataset with more than 6,000 neurons,[28] we categorized them into 11 cell types according to their soma regions, and sampled 100 cells from each cell type, forming a dataset with 1,100 cells (Table S11).

For training brain regions, we used 1,074 cells (from the 1,282 cells) as a training dataset and augmented it by adding four types of spatial Gaussian noise (mean = 0 μm, standard deviation = 5, 10, 15, and 20 μm, respectively). For each node, a random displacement is added to its spatial coordinate. After the augmentation, the total dataset contained 5,370 neurons.

To standardize the neuron reconstructions, we performed two preprocessing steps: small neuron segments, the length of which is less than 10 μm, were removed and the distance between adjacent connected nodes was readjusted to 20 μm (using "resample swc", a Vaa3D built-in plugin,[37] v.3.601).

Train brain regions to dense vectors

To utilize brain regions in neuron cell type analysis effectively, a proper method is needed to vectorize regions. One-hot encoding encodes categorical features by creating a binary column for each category. However, one-hot encoding not only fails to indicate the relationship of encoded vectors but also triggers dimension explosion if there are too many categories in a dataset. Thus, in natural language process tasks, W2V is commonly used to train word embeddings from one-hot encoding to dense vectors in a corpus.[22] The intuitive idea behind W2V is to gather similar words and disperse irrelevant words in their latent vector space. Since one-hot encodings of words are similar to brain regions in our case, it is easy to extend this method to train brain region encodings.

There are multiple model architectures to train W2V encodings. As illustrated in Figure 2A, we selected continuous bag-of-words as the W2V architecture. Initially, each word is encoded as 1-of-V vector using one-hot encoding, where V is the size of the vocabulary (all words in the corpus). Instead of feeding a whole sequence as input, we see each word (center word) and its neighboring words (context words, size = N) as an input-output pair, transferring a complete sequence into sub-sequences. The input layer projects context words (N × V data matrix) to the linear hidden layer (D-dimension latent space), using a weight matrix W (V × D, shared by N words). At the hidden layer, the N words embeddings are averaged as the center word representation (D-dimension, dense vector), which is also used to predict the 1-of-V vector of the center word. Given a one-hot encoding of input word, the W2V model gives its dense vector by multiplying matrix W.

For the classification task of local morphology (dendrites) from the 1,282 SEU dataset, we further divided cortical regions to laminar levels, finding that the detailed separation of brain regions can improve the performance of local morphology classification by 8% (Figure S7).

The W2V model is available in an open-source python library, Gensim[38] (v.3.7.0; API: gensim.models.Word2Vec; parameters; Table S1) for the training of vector embedding.

DSM-HAN for morphology classification

We explored alternative models to reach higher and more robust performance in classification. HAN[19] is a supervised classification algorithm to classify documents in NLP. Unlike traditional document classification treating the whole document as one continuous word sequence, HAN focuses on the structure of the document and builds representations of sentences that are then aggregated into a document representation.

The intuition of HAN is not classifying documents based on isolated words, but rather relating the task with the interaction of words. By transplanting the idea to neuron sequence, we introduce the DSM-HAN model, which decomposes a neuron sequence (a document) into segments (sentences) according to the topology of neuron structure, and treats each segment as a subsequence, representing local morphologies. The number of segments in each neuron sequence and the segment length (the number of nodes in each segment) are determined by their distributions (Figure S2).

The model architecture is summarized in Figure 3A. It has three parts: a word-level network (blue boxes), a sentence-level network (yellow boxes), and a classification network (orange boxes). The word- and sentence-level networks have basically the same architecture including a word sequence encoder (GRU, gated recurrent unit[39]), a word attention layer, and an average layer. The classification layer consists of several fully connected layers, outputting the probability estimation of cell types.

We used GRU to embed sequence data, and the attention layer to evaluate the importance of each state in a sequence and to add weight to them. The GRU belongs to the RNN family, with the ability to encode information from sequence data. Compared with traditional RNN, the GRU has two types of gates, reset gate r_j and update gate z_j, which are used for solving gradient vanishing in RNN-related training. At the j-th state of a sequence, the current hidden state h_j is computed by

$$h_j = z_j h_{j-1} + (1 - z_j)\tilde{h_j}$$

where update gate z_j decides the proportion of current candidate hidden state $\tilde{h_j}$ to previous hidden state h_{j-1} in current hidden state. The $\tilde{h_j}$ is computed as:

$$\tilde{h_j} = tanh\ (W_h x_j + U_h(h_{j-1} \odot r_j) + b_h\ )$$

where reset gate r_j balances the contribution between current input information and previous state information to candidate hidden state h_j.

The gates r_j and z_j are computed by

$$r_j = sigmoid(W_r x_j + U_r h_{j-1} + b_r)$$

$$z_j = sigmoid(W_z x_j + U_z h_{j-1} + b_z)$$

The attention layer, origin from the attention mechanism, gives prominence to important states in a sequence by assigning higher weights to them.

The mechanism filters out fewer relative words and causes contributing words to dominate in tasks. For the current state h_j, we have

$$u_j = tanh\left(W_w h_j + b_w\right)$$

$$\alpha_j = \frac{\exp\left(u_j^T u_w\right)}{\sum_j \exp\left(u_j^T u_w\right)}$$

$$s = \sum_j \exp\left(\alpha_j h_j\right)$$

where u_j is the embedding of each state h by one-layer multilayer perception, denoting the importance of each state, and α_j is the normalized weight of the state h_j. s is the weighted sequence embedding as the final output, and subscripts W, U, and b refer to trainable weights.

We built the DSM-HAN model using a TensorFlow[40] (v.2.4.0) framework.

DSM-AE for morphology representation

Traditionally, neuron morphologies are encoded by selecting features that are highly expert dependent and suffer from information loss inevitably. Here, we introduce the autoencoder model, which is an unsupervised neural network built for representation learning. The model aims to learn a latent representation of input neurons and reconstruct the original morphology from the latent representation.

The autoencoder architecture is summarized in Figure 4A. The model has two parts: encoder and decoder. The encoder part takes a neuron sequence as input, and encodes it into a reduced dimension vector, representing the neuron morphology; and the decoder is responsible for reconstructing the original input sequence from the reduced vector. Both encoder and decoder are composed of GRU layers, and they are connected by a RepeatVector (RV) layer. The RV layer simply repeats its input data, and we used it here to recover the sequence length. The implementation of DSM-AE is realized by TensorFlow[40] (v.2.4.0) framework.

We clustered the neurons with the encoder outputs. The clustering is performed using the Density-Based Spatial Clustering of Applications with Noise (DBSCAN) algorithm[30] under strict clustering policy (Figure S9). Specifically, the noise recognized by DBSCAN was removed first. This part is also realized by the "scikit-learn" python package[41] (v.1.0.2; API: sklearn.cluster.DBSCAN and sklearn.metrics.adjusted_rand_score; parameters, see clustering policy: Figure S9).

Quantification of the separation of 12 cell types is evaluated by the discriminability.[23] This part is realized by the python package "hyppo"[42] (v.0.3.2; API: hyppo.discrim.DiscrimOneSample; parameters, default).

The post-processing methods include z-score normalization, PCA, tSNE, UMAP, ISOMAP, MDS, and LLE, which are implemented by two python packages, including scikit-learn[41] (v.1.0.2; API: sklearn.preprocessing.StandardScaler, sklearn.decomposition.PCA, sklearn.manifold.Isomap, sklearn.manifold.LocallyLinearEmbedding, sklearn.manifold.MDS, and sklearn.manifold.TSNE; parameters, default) and the "umap-learn" python package[43] (v.0.5.3; API: umap.UMAP; parameters, default).

To provide predictions of cells similar to the input of the model, we converted the input cell sequence into a 32-dimension vector using the autoencoder model and used the Euclidean distance to recommend the top 4 cells.

Hyperparameter determination

To achieve high performance of DSM models, we tested rounds of hyperparameters and summarized the key results (Figure S2; Table S1).

For the hidden layer dimension of the W2V model (testing range, 1–80), we found that the validation accuracy of DSM-HAN exceeded 90% with hidden layer dimension >3 (Figure S2).

For DSM-HAN learning rate (LR), we fixed other parameters and trained DSM-HAN under different LR values (0.1, 0.01, 0.001, and 0.0001). With LR = 0.1, the training process resulted in overshooting where the training loss dramatically increased. With LR = 0.0001, the rate of convergence was low as the validation loss was still decreasing after 300 training iterations. With LR = 0.01 or 0.001, convergence was observed between 50 and 100 iterations. We conclude that LR is a crucial parameter for achieving high classification accuracy (Figure S13). The training of DSM-AE also follows the same procedure and shows similar results (Figure S13).

The hierarchical attention network is a commonly used model in the NLP area. The choice of the number of layers and dimensions has been in a previous study,[19] and we downsize the two parameters considering the capability of our device (GTX 2060Ti; Figure S2). We also suggest that users explore new combinations of these tunable parameters with the major design unchanged (Table S1).

We further tested a series of hidden layer dimensions for the DSM-HAN classification network, finding that the hidden layer dimensions hardly affect the final training results (Figure S13).

TFIDF for morphology classification

In the field of natural language processing, the basic form of data is the sequence. By transforming neuron reconstruction data to sequences, we can extend numerous methods from the NLP area to a cell-type classification task.

The acronym TFIDF stands for term frequency and inverse document frequency for a word. Term frequency is the number of times that a term occurs in a document (a neuron sequence), indicating the importance of the term to the document, and inverse document frequency is defined to measure how unique the word is to the document in documents, calculated by dividing the total number of documents by the number of documents containing the word and then taking the logarithm of that quotient.

To perform feature extraction, neuron sequences are regarded as documents, which were converted to a matrix of TFIDF features (number of documents × number of words), and then machine learning algorithms such as SVM can be used on the TFIDF matrix. The feature extraction was implemented using scikit-learn[41] (v.1.0.2; API: sklearn.feature_extraction.text.TfidfVectorizer; parameters, default).

Comparison with alternative approaches

The TMD framework[14,15] provides a flexible framework to vectorize neuron morphologies. In this study, we used the TMD python package (v.2.2.0; API: tmd.methods.get_persistence_diagram; parameters, default), using "radial distance" as description function, to calculate the TMD features (see https://github.com/BlueBrain/TMD for details).

NBLAST[13] provides a direct cell-cell comparison method by measuring pairwise neuronal similarity. We used the "NBLAST" R package (v.1.6.5; API: nblast; parameters, v.2, other parameters, default). We obtained the similarity between 1,282 cells, generating a similarity matrix (1,282 × 1,282).

The L-Measure features were acquired by "global_neuron_feature", a plugin of Vaa3D[37] (v.3.601). We collected 11 features from the results (Table S12).

The Sholl analysis[44] were performed by a python script "sholl analysis.py", which is archived on the Zenodo repository[36] (https://doi.org/10.5281/zenodo.8186904, see "neuron2seq_for_developer" folder; parameters, r_max: 10,000, and steps: 10).

Linear-kernel SVM, for neuronal morphology classification, is realized by the scikit-learn python package[41] (v.1.0.2; API: sklearn.linear_model.SGDClassifier; parameters, loss hinge; others, default).

TextCNN[27] was realized with three convolution layers (steps 2, 3, and 5), and followed by a "concatenate" layer. We used the concatenated vectors for cell classification. The codes are developed by TensorFlow[40] (v.2.4.0).

TextRNN[26] was realized with two GRU layers (dims 128 and 64) and followed by two densely connected layers for classification. The codes are developed by TensorFlow[40] (v.2.4.0).

GCN[25] was realized by three simple GCN layers (dims 128, 256, and 128), followed by a "global_mean_pool" layer. We used the pooling embeddings as neuron embeddings for classification. The codes are developed by Pytorch-Geometric[45] (v.2.1.0).

Outlier detection and automated dataset annotation

To identify unknown cell types, we developed an outlier detection module, combining both the DSM-AE and DSM-HAN models. Our results using DSM-HAN showed that we can provide a reliable cell-type identification for input cells within the 12 projections we studied, but classifying cells beyond the 12 classes was an unsolved problem. To address it, we trained 12 extra one-class SVMs as outlier detectors to correct the DSM-HAN predictions, assigning them to "unknown types" accordingly.

Taking the DSM-AE embeddings as the training dataset, we trained these one-class SVMs, predicting whether each cell is inside-class or outside-class for each cell type. We implemented the one-class SVMs using scikit-learn (v.1.0.2; parameters, default).

Analysis of co-expression genes in connected brain structures

We used a trained DSM-AE model to obtain embeddings of 1,282 cells, and clustered them using the DBSCAN algorithm (see Figure S9 for clustering policy; see Table S13 for unsupervised labeling). For each cell type, we sorted their target brain regions by projection strength, which is averaged over each target brain region; and, by accumulating the first N averaged projection strength until 90% of the total, we defined the first N brain regions as interconnected within this cell type (Figure S14). To binarize gene expression in target brain structures, for each Allen Brain Atlas[21] experiment we determined the threshold of gene expression as mean + 1 × standard deviation. To perform the functional enrichment analysis, we used the top 200 most frequently co-expressed genes or 6,169 expressed genes (Table S14) as input gene set. We used the enrichGO function of R package clusterProfiler (v.4.4.1).

SUPPLEMENTAL INFORMATION

Supplemental information can be found online at https://doi.org/10.1016/j.patter.2023.100896.

ACKNOWLEDGMENTS

This study was mainly supported by several grants awarded to H.P. from the Institute for Brain and Intelligence, Southeast University. H.P. was also supported by a Zhejiang Lab BioBit Program visiting grant (2022BCF07). This work was also partially supported by a National Science Foundation of China (NSFC) grant (U20A6005). P.X. was partially supported by NSFC grant 32100529. L.L. was partially supported by a grant from Tencent (8550270010). We also thank Giorgio Ascoli for the discussion and comments on the manuscript and various members of the BICCN Morphology Workgroup for feedback.

AUTHOR CONTRIBUTIONS

H.P. and P.X. conceptualized and supervised the project. H.P. and L.L. proposed and supervised the cell sub-typing and gene expression analysis studies. F.X. implemented W2V and deep neural networks. F.X., P.X., and Z.Z. performed the main data analysis with help from the co-authors. P.X., F.X., and H.P. wrote the manuscript with help and feedback from the co-authors. Y.L., F.X., and S.Z. double-checked and curated the projection types of 1,002 cells. L.L. led a team to generate the SEU morphology dataset. L.L. and L.M.-G. provided the cross-validation analysis for cell sub-typing. F.X., P.X., and H.P. performed gene expression analysis.

DECLARATION OF INTERESTS

The authors declare no competing interests.

Received: July 31, 2023
Revised: August 24, 2023
Accepted: November 20, 2023
Published: December 13, 2023

REFERENCES

1. Armañanzas, R., and Ascoli, G.A. (2015). Towards the automatic classification of neurons. Trends Neurosci *38*, 307–318.
2. Gouwens, N.W., Sorensen, S.A., Berg, J., Lee, C., Jarsky, T., Ting, J., Sunkin, S.M., Feng, D., Anastassiou, C.A., Barkan, E., et al. (2019). Classification of electrophysiological and morphological neuron types in the mouse visual cortex. Nat. Neurosci. *22*, 1182–1195.
3. Winnubst, J., Bas, E., Ferreira, T.A., Wu, Z., Economo, M.N., Edson, P., Arthur, B.J., Bruns, C., Rokicki, K., Schauder, D., et al. (2019). Reconstruction of 1,000 Projection Neurons Reveals New Cell Types and Organization of Long-Range Connectivity in the Mouse Brain. Cell *179*, 268–281.e13.
4. Peng, H., Xie, P., Liu, L., Kuang, X., Wang, Y., Qu, L., Gong, H., Jiang, S., Li, A., Ruan, Z., et al. (2021). Morphological diversity of single neurons in molecularly defined cell types. Nature *598*, 174–181.
5. Sadler, M., and Berry, M. (1983). Morphometric study of the development of Purkinje cell dendritic trees in the mouse using vertex analysis. J. Microsc. *131*, 341–354.
6. Glaser, E.M., and McMullen, N.T. (1984). The fan-in projection method for analyzing dendrite and axon systems. J. Neurosci. Methods *12*, 37–42.
7. Panico, J., and Sterling, P. (1995). Retinal neurons and vessels are not fractal but space-filling. J. Comp. Neurol. *361*, 479–490.
8. Guerra, L., McGarry, L.M., Robles, V., Bielza, C., Larrañaga, P., and Yuste, R. (2011). Comparison between supervised and unsupervised classifications of neuronal cell types: a case study. Developmental neurobiology *71*, 71–82.
9. Scorcioni, R., Polavaram, S., and Ascoli, G.A. (2008). L-Measure: a web-accessible tool for the analysis, comparison and search of digital reconstructions of neuronal morphologies. Nat. Protoc. *3*, 866–876.
10. Sümbül, U., Song, S., McCulloch, K., Becker, M., Lin, B., Sanes, J.R., Masland, R.H., and Seung, H.S. (2014). A genetic and computational approach to structurally classify neuronal types. Nat. Commun. *5*, 3512.
11. Hosp, J.A., Strüber, M., Yanagawa, Y., Obata, K., Vida, I., Jonas, P., and Bartos, M. (2014). Morpho-physiological criteria divide dentate gyrus interneurons into classes. Hippocampus *24*, 189–203.
12. Lu, Y., Carin, L., Coifman, R., Shain, W., and Roysam, B. (2015). Quantitative arbor analytics: unsupervised harmonic co-clustering of populations of brain cell arbors based on L-measure. Neuroinformatics *13*, 47–63.
13. Costa, M., Manton, J.D., Ostrovsky, A.D., Prohaska, S., and Jefferis, G.S. (2016). NBLAST: Rapid, Sensitive Comparison of Neuronal Structure and Construction of Neuron Family Databases. Neuron *91*, 293–311.
14. Li, Y., Wang, D., Ascoli, G.A., Mitra, P.P., and Wang, Y. (2016). Metrics for comparing neuronal tree shapes based on persistent homology. PLoS One *12*, 20182184.
15. Kanari, L., Dłotko, P., Scolamiero, M., Levi, R., Shillcock, J., Hess, K., and Markram, H. (2018). A Topological Representation of Branching Neuronal Morphologies. Neuroinformatics *16*, 3–13.
16. Wan, Y., Long, F., Qu, L., Xiao, H., Hawrylycz, M., Myers, E.W., and Peng, H. (2015). BlastNeuron for Automated Comparison, Retrieval and Clustering of 3D Neuron Morphologies. Neuroinformatics *13*, 487–499.
17. Gillette, T.A., and Ascoli, G.A. (2015). Topological characterization of neuronal arbor morphology via sequence representation: I--motif analysis. BMC Bioinf. *16*, 216.
18. Gillette, T.A., Hosseini, P., and Ascoli, G.A. (2015). Topological characterization of neuronal arbor morphology via sequence representation: II–global alignment. BMC Bioinf. *16*, 209.
19. Yang, Z., Yang, D., Dyer, C., He, X., and Hovy, E. (2016). Hierarchical Attention Networks for Document Classification. In Proceedings of the 2016 Conference of the North American Chapter of the Association for Computational Linguistics: Human Language Technologies, K. Knight, A. Nenkova, and O. Rambow, eds. (Association for Compuational Linguistics), pp. 1480–1489.
20. Wang, Q., Ding, S.L., Li, Y., Royall, J., Feng, D., Lesnar, P., Graddis, N., Naeemi, M., Facer, B., Ho, A., et al. (2020). The Allen Mouse Brain Common Coordinate Framework: A 3D Reference Atlas. Cell *181*, 936–953.e20.
21. Harris, J.A., Mihalas, S., Hirokawa, K.E., Whitesell, J.D., Choi, H., Bernard, A., Bohn, P., Caldejon, S., Casal, L., Cho, A., et al. (2019). Hierarchical organization of cortical and thalamic connectivity. Nature *575*, 195–202.
22. Mikolov, T., Chen, K., Corrado, G.S., and Dean, J. (2013). Efficient Estimation of Word Representations in Vector Space. Preprint at arXiv.
23. Bridgeford, E.W., Wang, S., Wang, Z., Xu, T., Craddock, C., Dey, J., Kiar, G., Gray-Roncal, W., Colantuoni, C., Douville, C., et al. (2021). Eliminating

accidental deviations to minimize generalization error and maximize replicability: Applications in connectomics and genomics. PLoS Comput. Biol. *17*, e1009279.

24. Salton, G., and Yu, C.T. (1974). On the construction of effective vocabularies for information retrieval. SIGPLAN Conferences and Workshops *9*, 48–60.

25. Kipf, T.N., and Welling, M. (2017). Semi-supervised classification with graph convolutional networks. Preprint at arXiv.

26. Liu, P., Qiu, X., and Huang, X. (2016). Recurrent Neural Network for Text Classification with Multi-Task Learning. Preprint at arXiv.

27. Kim, Y. (2014). Convolutional Neural Networks for Sentence Classification. In Proceedings of the 2014 Conference on Empirical Methods in Natural Language Processing (EMNLP), A. Moschitti, B. Pang, and W. Daelemans, eds. (Association for Computational Linguistics), pp. 1746–1751.

28. Gao, L., Liu, S., Gou, L., Hu, Y., Liu, Y., Deng, L., Ma, D., Wang, H., Yang, Q., Chen, Z., et al. (2022). Single-neuron projectome of mouse prefrontal cortex. Nat. Neurosci. *25*, 515–529.

29. Qu, L., Li, Y., Xie, P., Liu, L., Wang, Y., Wu, J., Liu, Y., Wang, T., Li, L., Guo, K., et al. (2022). Cross-modal coherent registration of whole mouse brains. Nat. Methods *19*, 111–118.

30. Ester, M., Kriegel, H., Sander, J., and Xu, X. (1996). A Density-Based Algorithm for Discovering Clusters in Large Spatial Databases with Noise (Proceedings of the Second International Conference on Knowledge Discovery and Data Mining. AAAI.), pp. 226–231.

31. Lein, E.S., Hawrylycz, M.J., Ao, N., Ayres, M., Bensinger, A., Bernard, A., Boe, A.F., Boguski, M.S., Brockway, K.S., Byrnes, E.J., et al. (2007). Genome-wide atlas of gene expression in the adult mouse brain. Nature *445*, 168–176.

32. Zhang, M., Eichhorn, S.W., Zingg, B., Yao, Z., Cotter, K., Zeng, H., Dong, H., and Zhuang, X. (2021). Spatially resolved cell atlas of the mouse primary motor cortex by MERFISH. Nature *598*, 137–143.

33. Richiardi, J., Altmann, A., Milazzo, A.C., Chang, C., Chakravarty, M.M., Banaschewski, T., Barker, G.J., Bokde, A.L., Bromberg, U., Büchel, C., et al. (2015). BRAIN NETWORKS. Correlated gene expression supports synchronous activity in brain networks. Science (New York, N.Y.) *348*, 1241–1244.

34. Mills, B.D., Grayson, D.S., Shunmugavel, A., Miranda-Dominguez, O., Feczko, E., Earl, E., Neve, K.A., and Fair, D.A. (2018). Correlated Gene Expression and Anatomical Communication Support Synchronized Brain Activity in the Mouse Functional Connectome. J. Neurosci. : the official journal of the Society for Neuroscience *38*, 5774–5787.

35. Goel, P., Kuceyeski, A., LoCastro, E., and Raj, A. (2014). Spatial patterns of genome-wide expression profiles reflect anatomic and fiber connectivity architecture of healthy human brain. Hum. Brain Mapp. *35*, 4204–4218.

36. Feng X. (2023). DSM: Deep Sequential Model for Complete Neuronal Morphology Representation and Feature Extraction. Zenodo. https://doi.org/10.5281/zenodo.8186904

37. Peng, H., Ruan, Z., Long, F., Simpson, J.H., and Myers, E.W. (2010). V3D enables real-time 3D visualization and quantitative analysis of large-scale biological image data sets. Nat. Biotechnol. *28*, 348–353.

38. Rehurek, R., and Sojka, P. (2010). Software Framework for Topic Modelling with Large Corpora. In Proceedings of the LREC 2010 Workshop on New Challenges for NLP Frameworks, pp. 45–50.

39. Cho, K., Merrienboer, B.V., Gülçehre, Ç., Bahdanau, D., Bougares, F., Schwenk, H., and Bengio, Y. (2014). Learning Phrase Representations using RNN Encoder–Decoder for Statistical Machine Translation. In Proceedings of the 2014 Conference on Empirical Methods in Natural Language Processing (EMNLP), A. Moschitti, B. Pang, and W. Daelemans, eds. (Association for Computational Linguistics), pp. 1724–1734.

40. Abadi, M., Agarwal, A., Barham, P., Brevdo, E., Chen, Z., Citro, C., Corrado, G.S., Davis, A., Dean, J., Devin, M., et al. (2015). TensorFlow: Large-scale machine learning on heterogeneous systems. Preprint at arXiv.

41. Pedregosa, F., Varoquaux, G., Gramfort, A., Michel, V., Thirion, B., Grisel, O., Blondel, M., Louppe, G., Prettenhofer, P., Weiss, R., et al. (2011). Scikit-learn: Machine Learning in Python. J. Mach. Learn. Res. *12*, 2285–2830.

42. Panda, S., Palaniappan, S., Xiong, J., Bridgeford, E.W., Mehta, R.R., Shen, C., and Vogelstein, J.T. (2019). hyppo: A Comprehensive Multivariate Hypothesis Testing Python Package. Preprint at arXiv.

43. McInnes, L., Healy, J., Saul, N., and Grossberger, L. (2018). UMAP: Uniform manifold approximation and projection. J. Open Source Softw. *3*, 861.

44. SHOLL, D.A. (1953). Dendritic organization in the neurons of the visual and motor cortices of the cat. J. Anat. *87*, 387–406.

45. Fey, M., and Lenssen, J.E. (2019). Fast graph representation learning with PyTorch Geometric. Preprint at arXiv.

Patterns, Volume *5*

Supplemental information

DSM: Deep sequential model for complete neuronal morphology representation and feature extraction

Feng Xiong, Peng Xie, Zuohan Zhao, Yiwei Li, Sujun Zhao, Linus Manubens-Gil, Lijuan Liu, and Hanchuan Peng

Supplemental Information

Supplemental Items

Supplemental Figures

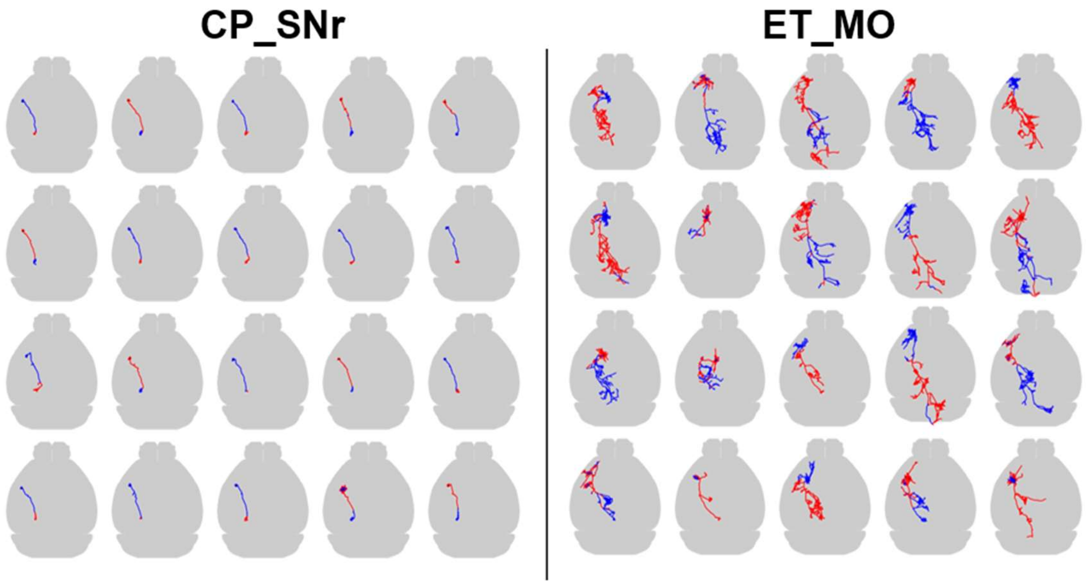

Figure S1. HAN segment-level encodings

Hierarchical clustering was performed for the HAN segment-level encodings for each cell, resulting in two clusters of segments corresponding to the first division of the hierarchical tree. Here we display the top-views of 40 neurons from two cell types, CP_SNr and ET_MO, and segments from same cluster are decorated by same color.

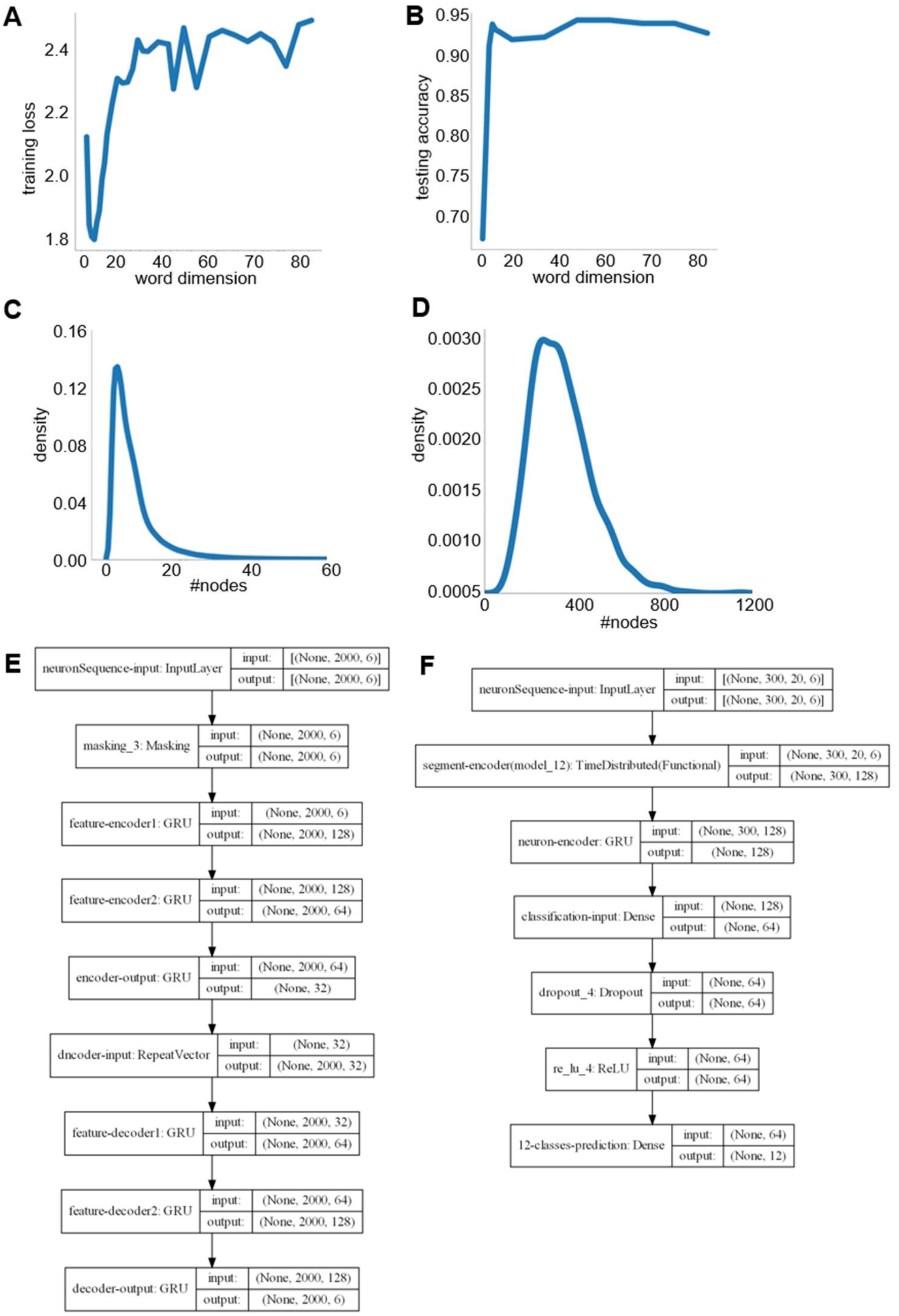

Figure S2. Training details of word2vec

A. Training loss of word2vec. X-axis indicates the dimension of hidden layer (the size of w2v encodings); Y-axis indicates training loss in the latest epoch. B. Testing accuracy of DSM- HAN under different W2V dimension. X-axis indicates the dimension of hidden layer (the size of w2v encodings); Y-axis indicates the testing of accuracy for DSM-HAN classification. C. The distribution of segment length. We used the mean value as the aligned segment length. D. The distribution of the number of segments in each neuron. We used the mean value as the aligned segment number. E. Architecture of DSM-HAN in this study. F. Architecture of DSM-AE in this study.

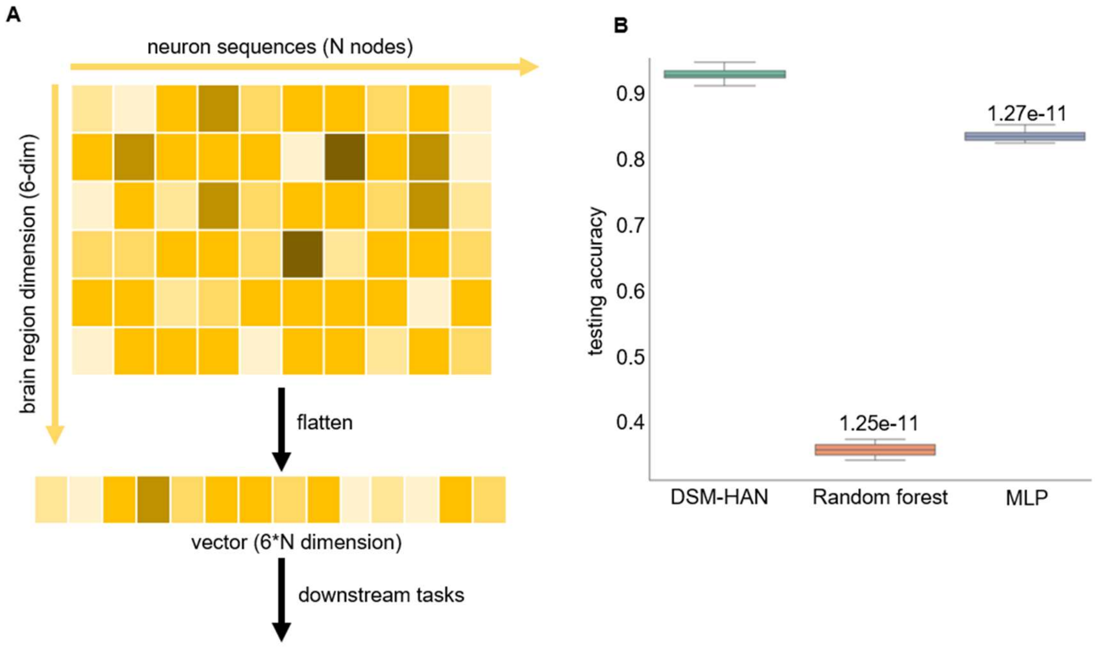

Figure S3. Comparison between HAN and simple classifiers on direct WV2 sequences

A. Flatting word2vec encoding sequences as vectors, we applied downstream analysis, including classification, clustering, and representation analysis on them. B. The classification comparison between DSM-HAN and simple classifiers, including random forest, and multilayer perceptron (numbers above box: P-Values of the Mann-Whitney U rank test (one-side) on test accuracy between DSM-HAN and others).

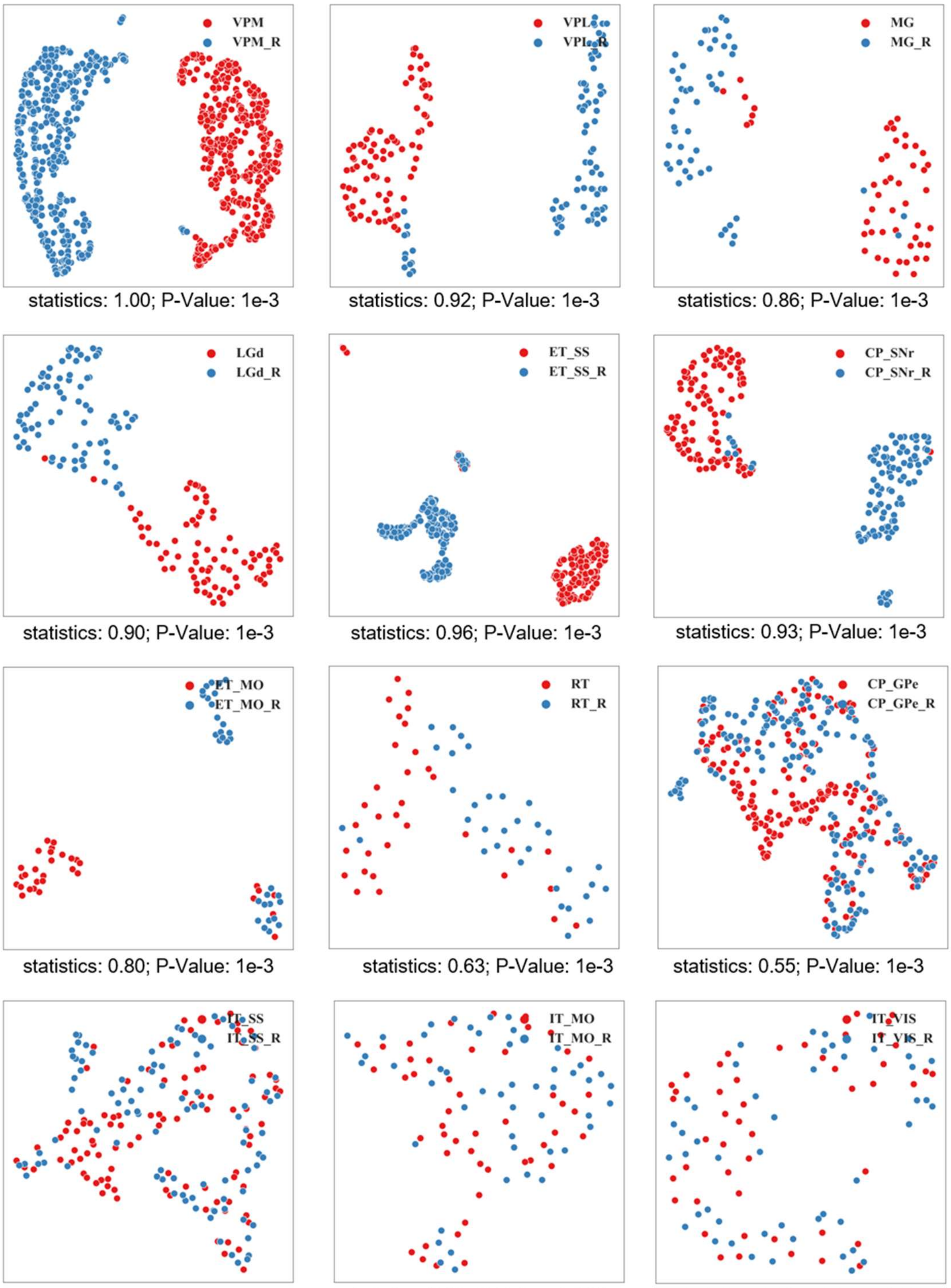

statistics: 1.00; P-Value: 1e-3

statistics: 0.92; P-Value: 1e-3

statistics: 0.86; P-Value: 1e-3

statistics: 0.90; P-Value: 1e-3

statistics: 0.96; P-Value: 1e-3

statistics: 0.93; P-Value: 1e-3

statistics: 0.80; P-Value: 1e-3

statistics: 0.63; P-Value: 1e-3

statistics: 0.55; P-Value: 1e-3

statistics: 0.51; P-Value: 4e-3

statistics: 0.51; P-Value: 0.130

statistics: 0.50; P-Value: 0.52

Figure S4. Clustering of HAN neuronal encodings for cells with or without sequence reverse

Each dot represents a neuron and each plot shows the results of UMAP dimension reduction. Here, we tested all the 1,282 cells from twelve cell types (from the SEU dataset) and colored original (red) and reversed (blue) cells. The statistics and P-Values of one-side 'One Sample Discriminability test' are displayed below the plots.

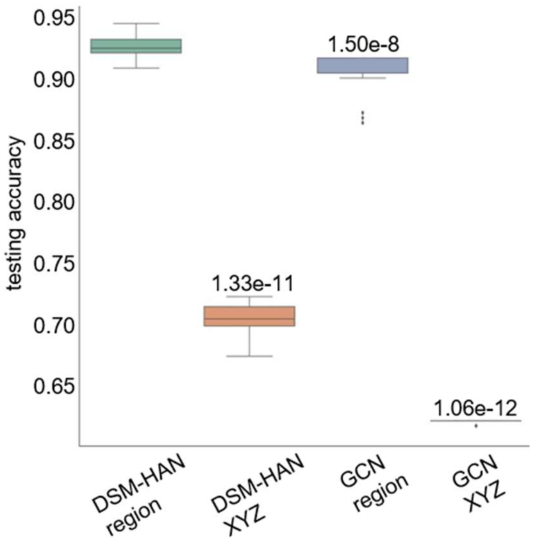

Figure S5. Comparison between brain region features and direct node coordinates

The comparison between our brain region features (W2V encodings), and node coordinates (X-Y-Z) using DSM-HAN on the SEU dataset. Our brain region feature achieved the higher classification accuracy (92.76%), while the other is 71.44% (numbers above box: P-Values of the Mann-Whitney U rank test (one-side) on test accuracy between two features).

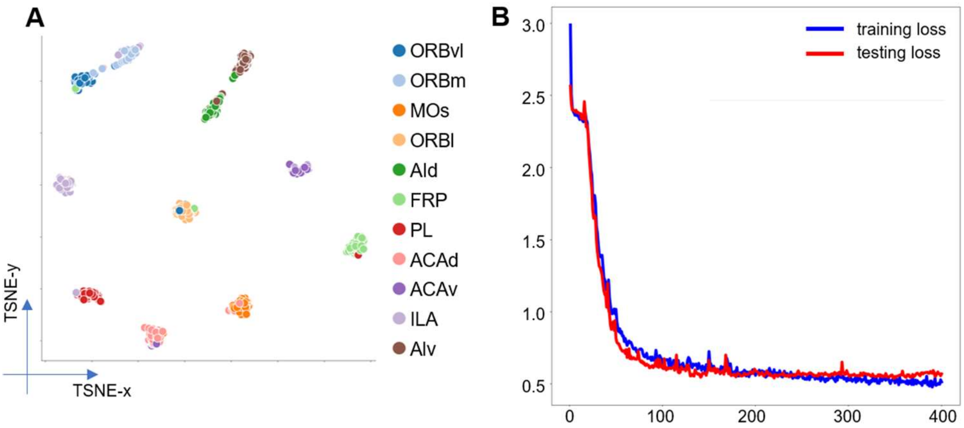

Figure S6. Classification in the 1,100 cells including 11 cell types

A. UMAP embeddings of the 1,100 cells encoded by DSM-HAN (average testing accuracy, 92.2%). B. Training process of DSM-HAN on the new dataset.

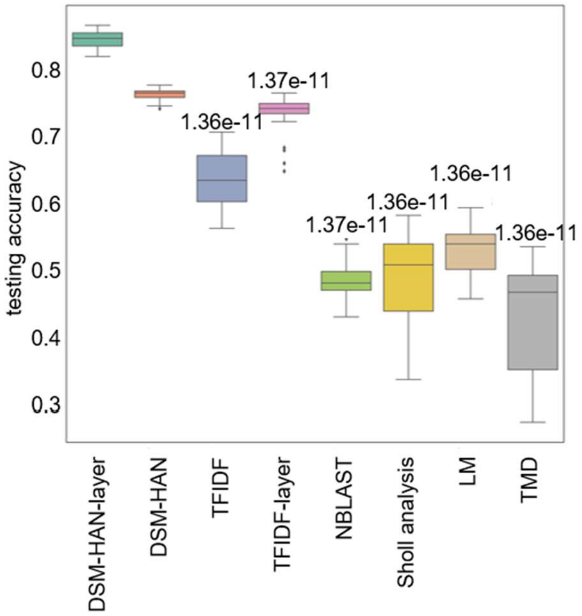

Figure S7. The comparison between DSM-HAN and alternative methods on the local morphology

Local morphologies are dendrites from SEU dataset, and DSM-HAN achieved the highest classification accuracy (76.4%). Accuracy of alternative approaches: TF-IDF = 63.8%, NBLAST = 48.6%, Sholl analysis = 49.5%, L-measure = 53.0%, TMD = 43.0%. We further refined brain region assignment considering layers of brain regions, and received accuracy of DSM-HAN-layer, 84.7%, and TFIDF-layer, 73.6% (numbers above box: P-Values of the Mann-Whitney U rank test (one-side) on test accuracy between DSM-HAN and respective method).

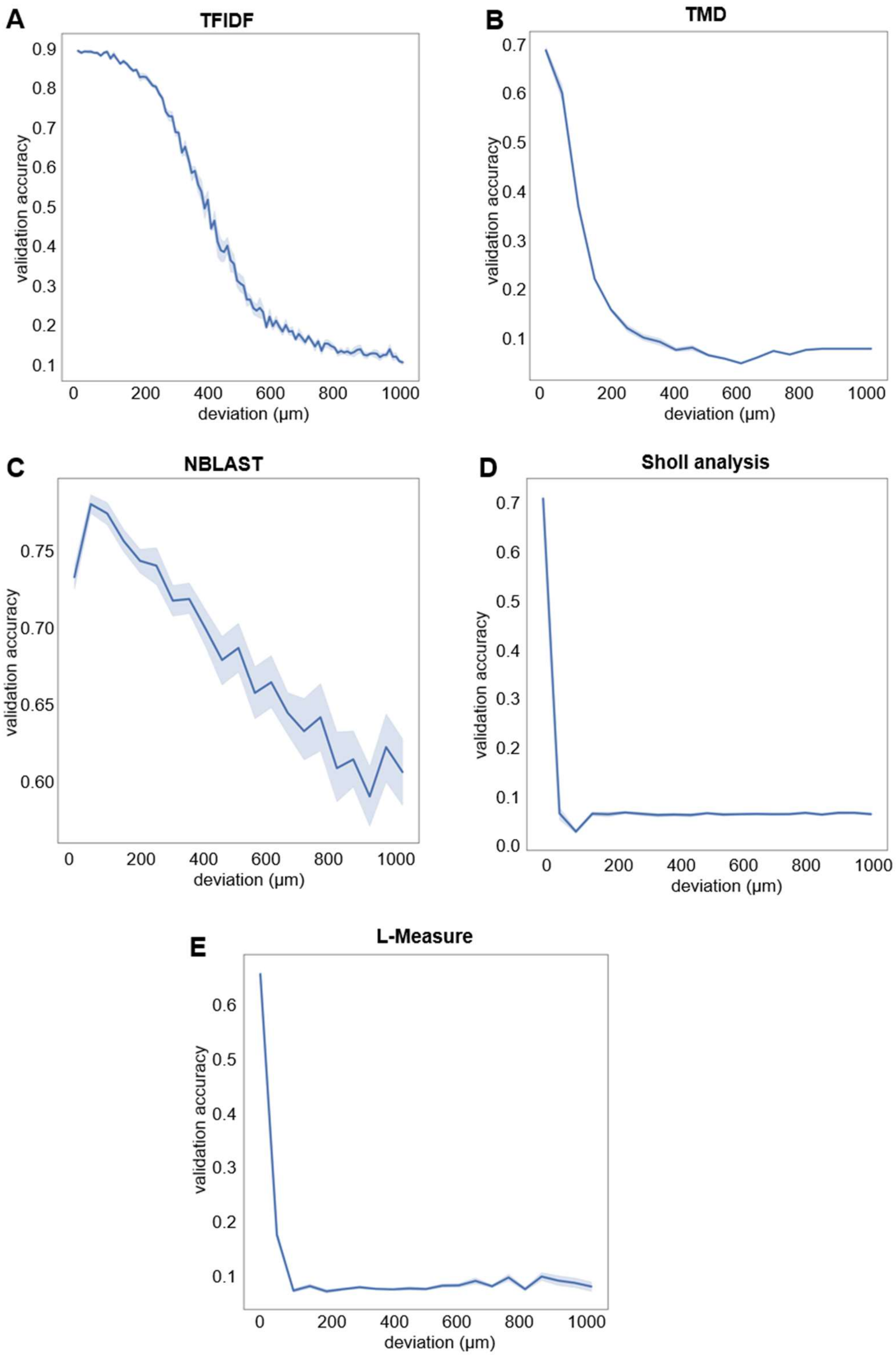

Figure S8. Comparison of robustness for alternative approaches

A-E. The robustness test to spatial noises for alternative approaches (TFIDF, TMD, NBALST, Sholl Analysis, and L-Measure). The Gaussian noises (mean = 0mm) were applied on these neuron reconstruction coordinates, with noise level (the standard deviation of Gaussian distribution) gradually increased from 10mm to 1000mm (step size: 50mm). Testing results indicated that TFIDF and NBLAST were able to maintain their accuracy under spatial noise < 100 mm, while the performance of others fell dramatically.

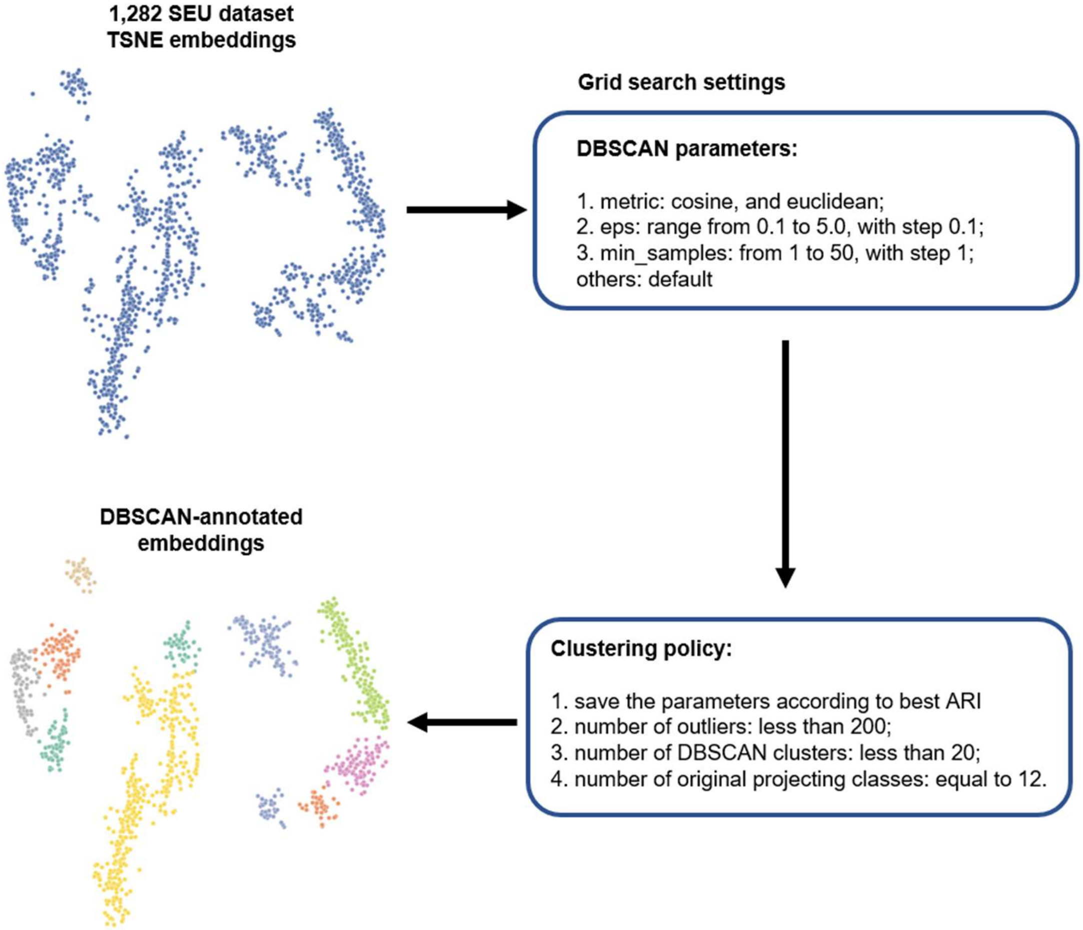

DBSCAN parameters:

1. metric: cosine, and euclidean;
2. eps: range from 0.1 to 5.0, with step 0.1;
3. min_samples: from 1 to 50, with step 1;

others: default

Clustering policy:

1. save the parameters according to best ARI
2. number of outliers: less than 200;
3. number of DBSCAN clusters: less than 20;
4. number of original projecting classes: equal to 12.

Figure S9. Clustering policy for DBSCAN algorithm

We pre-define parameter space for grid searching, and the input embeddings are passed to DBSCAN for clustering according the policy. The best clustering results were saved for annotating.

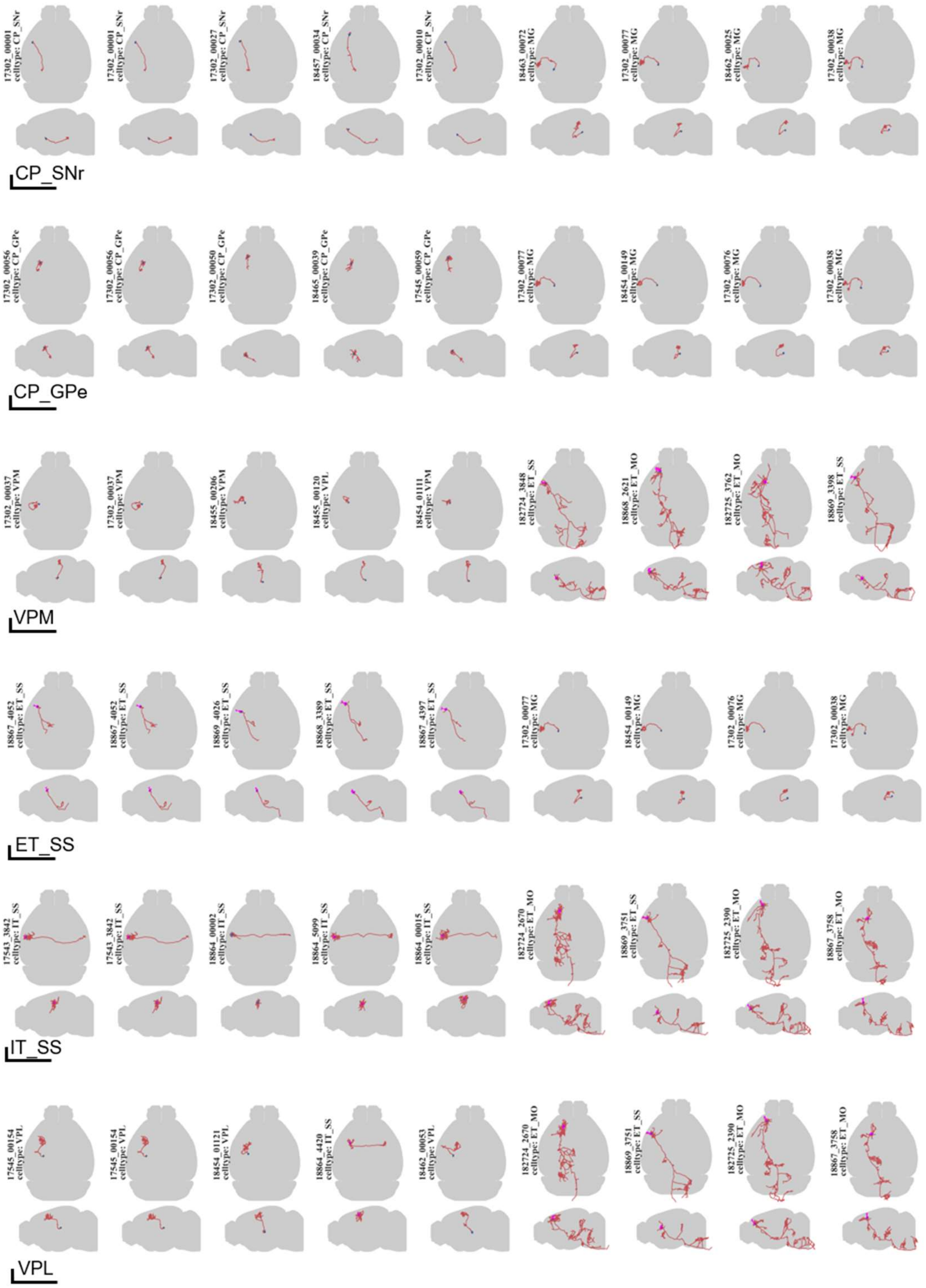
17302_00001 celltype: CP_SNr
17302_00001 celltype: CP_SNr
17302_00027 celltype: CP_SNr
18457_00034 celltype: CP_SNr
17302_00010 celltype: CP_SNr
18463_00072 celltype: MG
17302_00077 celltype: MG
18462_00025 celltype: MG
17302_00038 celltype: MG
CP_SNr
17302_00056 celltype: CP_GPe
17302_00056 celltype: CP_GPe
17302_00050 celltype: CP_GPe
18465_00039 celltype: CP_GPe
17545_00059 celltype: CP_GPe
17302_00077 celltype: MG
18454_00149 celltype: MG
17302_00076 celltype: MG
17302_00038 celltype: MG
CP_GPe
17302_00037 celltype: VPM
17302_00037 celltype: VPM
18455_00206 celltype: VPM
18455_00120 celltype: VPL
18454_01111 celltype: VPM
182724_3848 celltype: ET_SS
18868_2621 celltype: ET_MO
182725_3762 celltype: ET_MO
18869_3398 celltype: ET_SS
VPM
18867_4052 celltype: ET_SS
18867_4052 celltype: ET_SS
18869_4026 celltype: ET_SS
18868_3389 celltype: ET_SS
18867_4397 celltype: ET_SS
17302_00077 celltype: MG
18454_00149 celltype: MG
17302_00076 celltype: MG
17302_00038 celltype: MG
ET_SS
17543_3842 celltype: IT_SS
17543_3842 celltype: IT_SS
18864_00002 celltype: IT_SS
18864_5099 celltype: IT_SS
18864_00015 celltype: IT_SS
182724_2670 celltype: ET_MO
18869_3751 celltype: ET_SS
182725_2390 celltype: ET_MO
18867_3758 celltype: ET_MO
IT_SS
17545_00154 celltype: VPL
17545_00154 celltype: VPL
18454_01121 celltype: VPL
18864_4420 celltype: IT_SS
18462_00053 celltype: VPL
182724_2670 celltype: ET_MO
18869_3751 celltype: ET_SS
182725_2390 celltype: ET_MO
18867_3758 celltype: ET_MO
VPL

Figure S10. Cell retrieval examples

For the cell retrieval task, we provide both target cells and not-target cells for query cell, illustrating the diversity of neuron morphologies in this dataset and that this is also captured by our method. Columns 1 represents input cell, columns 2-4 represent target cells , and columns 6-9 represent non-target cells.

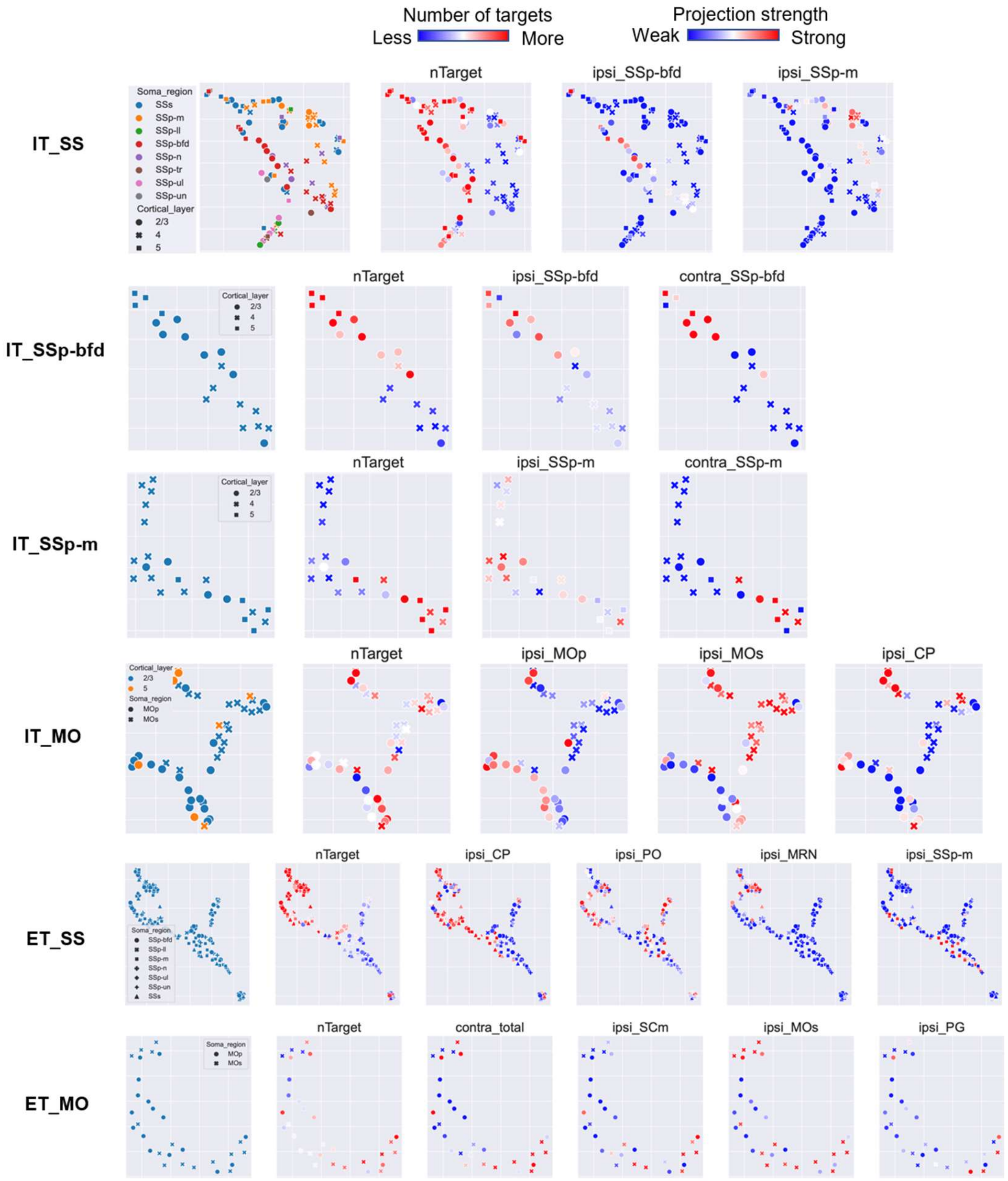

Figure S11. Re-clustering analysis for 6 cell-types of the SEU dataset

Re-clustering was operated on the DSM-AE representation of neurons. For each cell-type, the UMAP layout was shown. Soma region, cortical layers or projection sub-types were indicated by categorical colors or shapes. Number of targets and projection strength of representative target regions were represented gradient colors. For IT_SS cells, re-clustering of two sub-types (IT_SSp-bfd and IT_SSp-m) was shown.

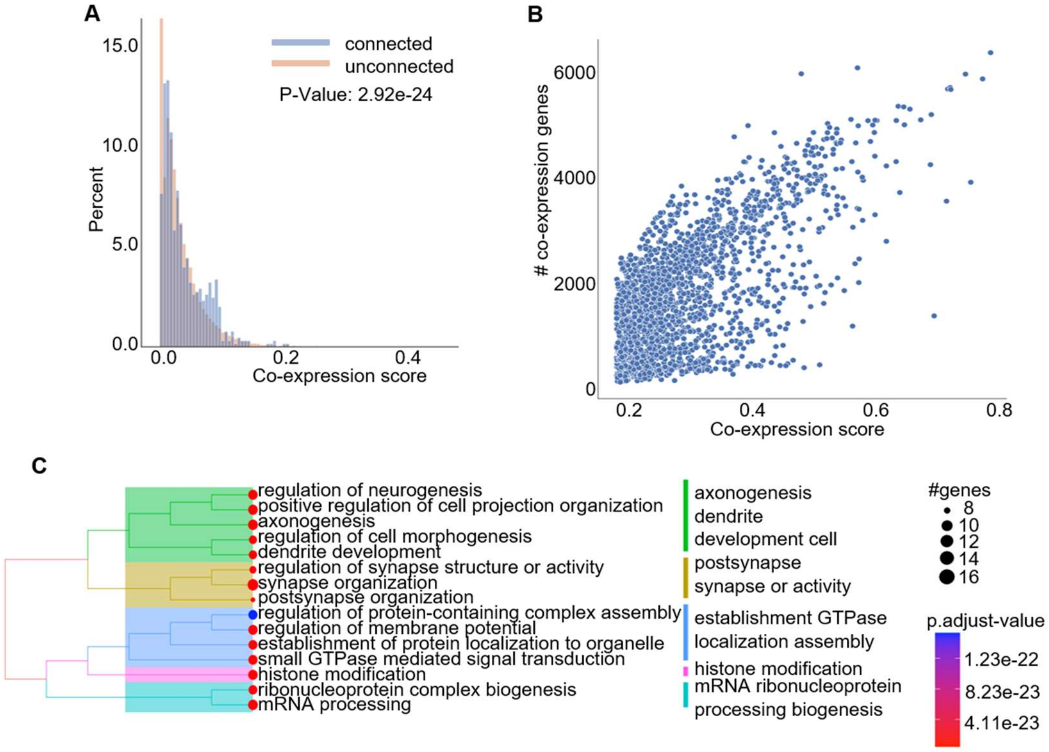

Figure S12. Supplemental co-expression analysis

A. Histogram for the distribution of co-expression scores of connected and unconnected brain regions pairs, which are from different major brain region. 'Percent' indicates the percent of observations that fall within a specific bin. Colors represent brain regions' state (P-Value: 2.92e-24, two-sided KS test). B. Co-expression brain regions. Scatterplot of 2,251 pairs of connected regions with strong co-expression (selected by co-expression score, threshold 0.180). The x- and y-axis represent co-expression scores and the numbers of co-expression genes. C. Functional enrichment analysis of genes expressed in the brain atlas. GO tree-plot results show the clustering of top-15 enriched functional terms (adjusted P-Values, hypergeometric test, 'BH' correction).

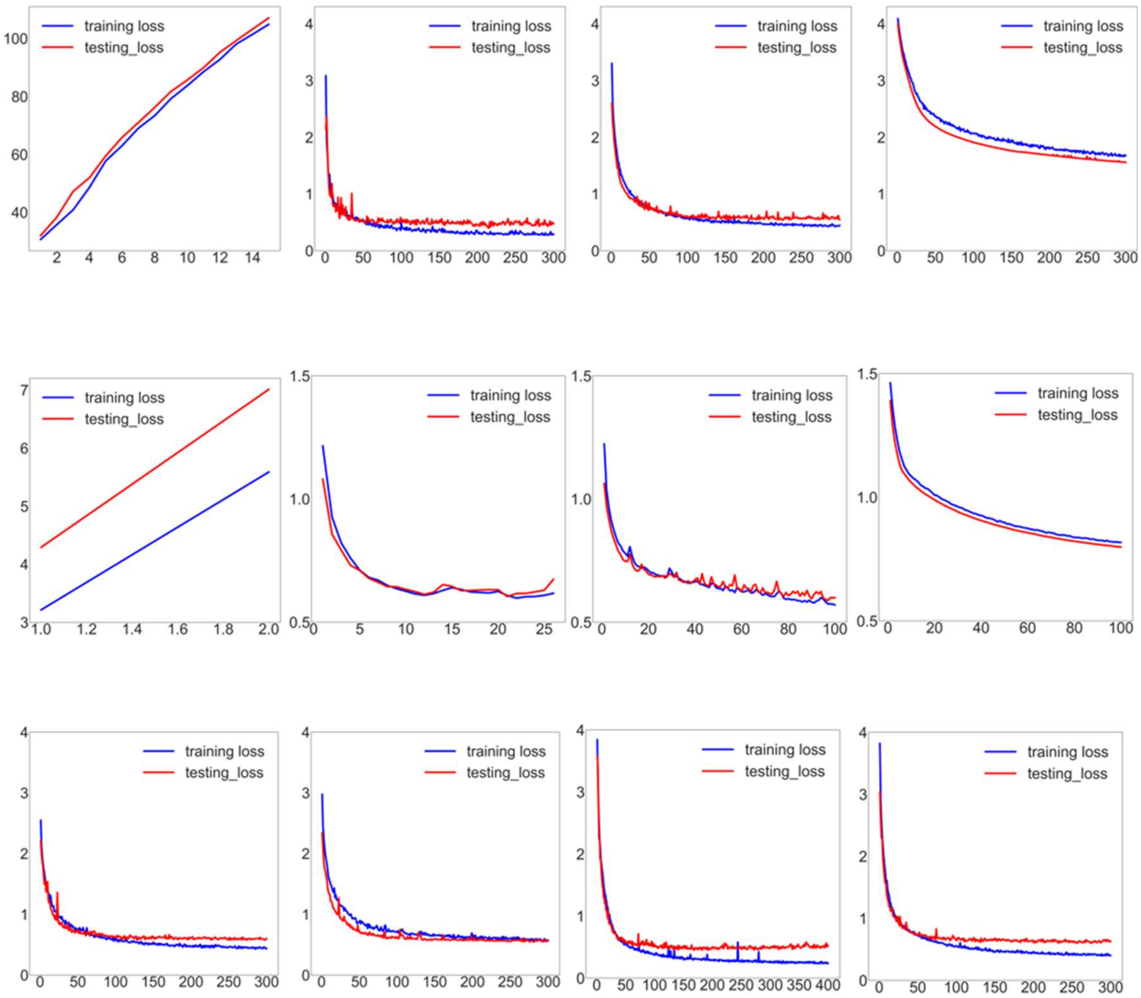

Figure S13. Training details of DSM-HAN

A. Learning rate tests for training of DSM-HAN model. From left to right, learning rate significantly affects the convergence of training. With LR=0.1, the training loss dramatically increased. With LR=0.0001, the rate of convergence was low as the validation loss was still decreasing after 300 training iterations. With LR=0.01 or 0.001, reasonable convergence can be observed. B. Learning rate tests for training of DSM-AE model. C. The classification performance under different hidden layer dimensions of classification network (dim = 16, 32, 64, 128). We found that this parameter can hardly affects the performance.

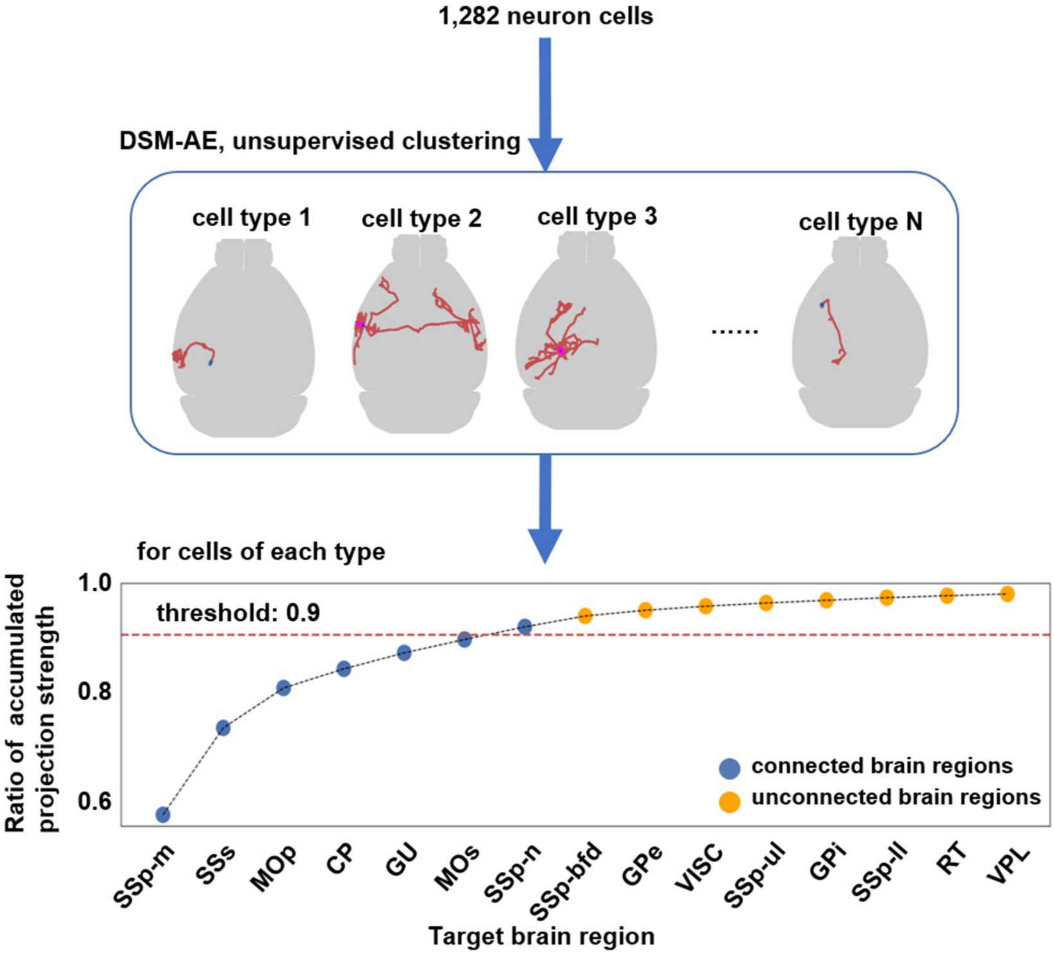

Figure S14. Policy for determining brain region connection

To retrieve the brain region connections at whole mouse brain level, we first identified the 1,282 neuron cells into 11 clusters, using DSM-AE embeddings and DBSCAN algorithm. For each cell type, we reordered their target brain regions in descending order by averaged projection strength (from left to right). By accumulating the first N averaged projection strength until 90% of total projection strength, the first N regions are defined as connected. The regions below blue dots represent connected regions, while the regions below orange dots are unconnected regions.

Supplemental Tables

Table S4. The measurements of ARI and discriminability on DSM-AE representations. The correspondence of clusters and cell types is evaluated by ARI, and we calculate the ARI metric under alternative post-processing methods. The quantification of DSM-AE representation, is evaluated by discriminability, which also takes post-processing methods into consideration.

	Standardization	PCA	ISOMAP	MDS	LLE	UMAP	TSNE
DSM-AE	**0.577**	**0.549**	**0.605**	**0.544**	**0.592**	**0.677**	**0.719**
TFIDF	0.105	0.252	0.486	0.423	0.408	0.400	0.459
NBLAST	0.107	0.001	0.170	0.006	0.045	0.018	0.207
TMD	0.092	0.065	0.201	0.065	0.451	0.336	0.501
Sholl analysis	0.000	0.001	0.006	0.002	0.007	0.013	0.004
L measure	0.042	0.128	0.525	0.036	0.535	0.620	0.665
flatten neuron sequence	0.144	0.145	0.468	0.002	0.060	0.384	0.553

Table S6. Outlier detector performance.
An outlier detector is trained to filter unknown cells (not belong to the 12 classes). The training is performed on SEU dataset, and the testing is on Janelia dataset.

Celltype	**num_cells**	**HAN_prediction**	**outlier_detection_correction**	Note: training dataset comes from seu(1282 cells)
VPM	378	386	356	
VPL	80	73	57	
IT_MO	48	51	51	
ET_MO	31	29	24	
IT_VIS	48	47	39	
ET_SS	159	162	159	
IT_SS	97	95	82	
MG	50	50	36	
CP_GPe	180	180	166	
CP_SNr	100	97	79	
LGd	78	78	72	
RT	33	34	25	
(sum)	1282	1282	1146	

Table S12. Summary of 22 L-Measure features used in this study.

Number of Nodes
Soma Surface
Number of Stems
Number of Bifurcations
Number of Branches
Number of Tips
Overall Width
Overall Height
Overall Depth
Average Diameter
Total Length
Total Surface
Total Volume
Max Euclidean Distance
Max Path Distance
Max Branch Order
Average Contraction
Average Fragmentation
Average Parent-daughter Ratio
Average Bifurcation Angle Local
Average Bifurcation Angle Remote
Hausdorff Dimension